

EFFECT OF PRE-EXISTING HETEROGENEITIES ON STRAIN  
LOCALIZATION IN A FOLIATED GRANITIC GNEISS

A Thesis

Presented to

The Graduate Faculty of The University of Akron

In Partial Fulfillment

of the Requirements for the Degree

Master of Science

Jonathan Kullberg

May, 2021

EFFECT OF PRE-EXISTING HETEROGENEITIES ON STRAIN  
LOCALIZATION IN A FOLIATED GRANITIC GNEISS

Jonathan Kullberg

Thesis

Approved:

Accepted:

---

Advisor  
Dr. Caleb W. Holyoke, III

---

Acting Dean  
Dr. Joe Urgo

---

Faculty Reader  
Dr. John A. Peck

---

Interim Director of Graduate School  
Dr. Marnie Saunders

---

Faculty Reader  
Dr. David N. Steer

---

Date

---

Department Chair  
Dr. David N. Steer

## ABSTRACT

While Earth's crust is often modelled as a homogenous material, heterogeneities such as foliations, lattice preferred orientations (LPOs), and pre-existing brittle deformations are common and may affect the strength of the crust. To investigate the effects of pre-existing heterogeneities on crust strength, axial compression experiments were performed on pre-faulted samples of a fine-grained ( $d = 150\mu\text{m}$ ) gneiss (Gneiss Minuti) with a granitic composition consisting of plagioclase (53%), quartz (29%), potassium feldspar (10%), biotite (7%) and accessory garnet/Fe-Ti oxides (1%). Cores with varied orientations of foliation and lineation to the compression direction were deformed in a Griggs-type piston rock deformation apparatus in order to determine if these heterogeneities would affect the strength or localization in a pre-existing fault. An initial brittle fault that cross-cuts the foliation was formed in all samples at low confining pressure ( $P_c = 50 - 250 \text{ MPa}$ ) and temperatures ( $T = \sim 25^\circ\text{C}$ ). Samples were then brought to final conditions,  $P_c = 1500 \text{ MPa}$ ,  $T = 700^\circ\text{C}$ , and deformed at a constant axial strain rate of  $\sim 2 \times 10^{-7} \text{ s}^{-1}$ . At final conditions, the fine-grained fault gouge of the brittle fault was annealed and subsequently deformed by diffusion-accommodated grain boundary sliding within the shear zone, regardless of foliation orientation. Strain remained localized along the shear zone until strains of at least  $\sim 12 - 15\%$ , and the strain rate of the low to mid strain samples within the shear zone was calculated to be  $\sim 10^{-5} \text{ s}^{-1}$ . In a sample deformed to higher strain (44%) the surrounding rock began to deform via dislocation creep. The results of this study suggest that strain localization will most likely be controlled by a pre-existing fault, regardless of the orientation of the foliation in the surrounding host rock.

## ACKNOWLEDGEMENTS

I would like to thank my advisor Dr. Caleb Holyoke, whose knowledge and support made the process of completing this thesis an overall positive experience. I would also like to thank Dr. John Peck, whose feedback throughout my time at the University of Akron has improved my abilities as a scientific writer. I also extend much gratitude to Tom Quick for helping me through various issues on more occasions than I can count.

## TABLE OF CONTENTS

	Page
LIST OF FIGURES .....	vii
LIST OF TABLES .....	viii
CHAPTER	
I. INTRODUCTION .....	1
II. METHODS .....	4
2.1. Starting material .....	5
2.2. Sample assembly and apparatus .....	9
2.3 Experimental conditions .....	9
2.4 Mechanical data and sample analysis .....	11
III. RESULTS.....	13
3.1. Mechanical data .....	16
3.2. Microstructures .....	19
3.2.1. Hydrostatic.....	19
3.2.2. Low strain experiments.....	22
3.2.3. Intermediate strain experiments.....	25
3.2.4. High strain experiment.....	25
IV. DISCUSSION.....	29
4.1. Deformation mechanisms .....	29
4.2. Shear strain analysis.....	34
4.3. Shear localization.....	36
4.4. General implications .....	38

V. CONCLUSIONS.....	39
REFERENCES .....	41
APPENDICES .....	44
APPENDIX A: LIST OF EXPERIMENTS .....	45
APPENDIX B: SELECTED EXPERIMENTS NOT USED IN THE MAIN STUDY .....	47
APPENDIX C: MAGNETIC ANISOTROPY OF GNEISS MINUTI.....	57

## LIST OF FIGURES

Figure		Page
1	Schematic of Gneiss Minuti showing foliation and lineation.....	.6
2	Gneiss Minuti starting material.....	.7
3	Quartz lattice preferred orientation (LPO) in the Gneiss Minuti.....	.8
4	Schematic of sample assembly used in all experiments.....	.10
5	Low strain mechanical data.....	.17
6	Intermediate and high strain experiments mechanical data.....	.18
7	Fault in Enfield Aplite.....	.20
8	Short hydrostatic experiment.....	.21
9	Long hydrostatic experiment.....	.23
10	Low strain experiments.....	.24
11	Intermediate strain experiments.....	.26
12	Lower magnification images of the highly strained sample.....	.27
13	Higher magnification images of the highly strained sample.....	.28
14	Peak differential stresses vs. orientation.....	.30

## LIST OF TABLES

Table		Page
1	Orientation, strain, and peak stress for all experiments.....	14
2	Strain and pre-hit deformation data.....	15
3	Shear strain calculations.....	35

## CHAPTER I

### INTRODUCTION

With increasing depth within Earth's crust, changes in pressure and temperature cause changes in the active deformation mechanisms that occur during deformation (Sibson, 1977). Nearer to the surface, the crust deforms by brittle faulting, but deeper in the crust, ductile and crystal plastic mechanisms dominate. Models of the deformation of Earth's crust are often based on two components (Sibson, 1977; Bürgmann and Dresen, 2008): the strength of the upper crust is controlled by its resistance to frictional sliding with increasing pressure (e.g., Byerlee, 1978). The strength of the mid to lower continental crust below the brittle/ductile transition is controlled by quartz flow laws obtained through the experimental deformation of homogenous quartz aggregates (e.g., Gleason and Tullis, 1995; Hirth et al., 2001). However, heterogeneities within the crust are likely to cause deviations from these simplistic models of crustal deformation. For example, it has been shown that the orientation of foliations can have a significant effect on the strength of rocks when deformed by brittle mechanisms (Gottschalk et al., 1990; Shea and Kronenberg, 1993). Mica grains in orientations that maximize shear stress create stress concentrations which result in strength anisotropy. Stress concentrations at mica tips have also been observed to change the dominant deformation mechanism of granitic rocks (Holyoke and Tullis, 2006). Several studies have also demonstrated how the lattice preferred orientation (LPO) of olivine affects its strength and/or evolution of fabric when it is subjected to deformation by dislocation creep (Hansen et al., 2012; Boneh and Skemer, 2014; Hansen et al., 2016)

Besides mineral heterogeneities, foliations, and LPO's, another common crustal heterogeneity is a pre-existing brittle structure, such as a fault or joint which have higher porosity and/or a finer grain size caused by cataclasis. In natural rocks, it has been observed that ductile shear zones were initiated by the presence of a pre-existing brittle feature (e.g., Mitra, 1984; Segall and Simpson, 1986; Guermani and Pennacchioni, 1998; Mancktelow and Pennacchioni, 2005). Subsequent ductile deformation is a result of fluid influx due to increased porosity caused by the brittle deformation, causing mineralization and/or hydrolytic weakening, which can occur during the development of natural shear zones (Segall and Simpson, 1986; Kronenberg et al., 1990). However, ductile shear zones with brittle precursors have also been observed without evidence for alteration by fluid influx. Goodwin and Wenk (1995) observed a natural shear zone with a brittle pre-cursor that was found to be initiated solely by grain size reduction caused by cataclasis. Tullis et al. (1990) demonstrated this concept by experimentally deforming pre-faulted feldspar aggregates and feldspathic rocks under conditions that would cause the intact samples to deform homogeneously by dislocation creep. They observed that strain localized in the faults within the feldspathic rocks, resulting in a ductile shear zone. However, strain did not localize along the pre-existing fault in samples of quartzite, which deformed homogeneously. They concluded that the dislocation creep recovery methods that operate within quartz and feldspar determine if strain will localize along a pre-existing fault. Recrystallization-accommodated dislocation creep, which occurs in feldspar at the given experimental conditions, results in strain weakening with a decrease in grain size while climb-accommodated dislocation creep occurring in quartz does not.

These results indicate that feldspar plays a crucial role in the development of some ductile shear zones. Due to its two cleavage planes, and slow diffusion rates that make dislocation glide difficult, feldspar is susceptible to microcracking over a wide range of conditions (Tullis and Yund, 1987). Therefore, feldspar can easily form very fine-grained

(<0.1  $\mu\text{m}$ ) fault gouge that deforms by either recrystallization-accommodated dislocation creep or diffusion creep (Tullis and Yund, 1991). Fine-grained feldspar deforming by either mechanism will be much weaker than coarser grained feldspar at the same conditions, which can result in strain localization (Tullis and Yund, 1991). Thus, ductile shear zones in feldspathic rocks may easily develop due to initial grain size reduction caused by cataclasis and subsequent deformation by crystal plastic mechanisms activated by the decreased grain size, which causes strain weakening and localization. However, what is not entirely clear is the how other pre-existing heterogeneities (i.e., foliations, lineations, LPOs) may affect this localization. In this study, I seek to determine if the foliation, lineation, or LPO of a fine-grained granitic gneiss with a high feldspar content (Gneiss Minuti) affects ductile strain localization along a pre-existing brittle fault.

## CHAPTER II

### METHODS

In order to determine the effects that foliation and lineation orientation in the host rock have on strain localization in a pre-existing fault, I performed experiments on pre-faulted cores of the Gneiss Minuti in a Griggs – type piston rock deformation apparatus at  $T = 700^{\circ}\text{C}$ ,  $P_c = 1.5 \text{ GPa}$ , and  $\dot{\epsilon} = 10^{-7} \text{ s}^{-1}$  (Table 1). I have also performed additional experiments on the Gneiss Minuti to determine the pressure and temperature conditions necessary to avoid metamorphic reactions. All experiments performed, including those not discussed in this study, are listed in Appendix A. Some selected figures from experiments that are not included in this portion of my thesis are presented in Appendix B. The orientation of the brittle faults that formed in the samples was approximately  $25^{\circ}$  to the compression direction and cross cut the foliation in most cores. The angle between the foliation/lineation and the pre-existing fault was varied by pre-faulting cores of the Gneiss Minuti with different foliation and lineation orientations. If the foliation affects the strength of these cores, the cores will likely be weakest when deformed with the foliation oriented at  $45^{\circ}$  to the compression direction and strongest with foliation perpendicular to the compression direction. If the lineation affects the strength of these cores, those with the  $\langle a \rangle$  axes oriented in an easy slip direction will likely be weaker than those with the  $\langle a \rangle$  axes in a hard orientation. If the faults affect the strength of these cores, the strengths should be independent of the orientation of the foliation/lineation. If the strength is found to have a pattern in relation to the orientation of the foliation and/or lineation, it would indicate that the presence of the fault is unimportant to the strength of the rock.

Throughout my thesis, I refer to the faults caused by brittle deformation at low pressure and temperature as faults. After these faults have been deformed at high temperature and pressure, I refer to these faults as shear zones.

## 2.1. Starting material

Cylinders (~5 x 10 mm) were cored from the Gneiss Minuti at five orientations in relation to the foliation and lineation (Fig. 1). The Gneiss Minuti is a fine grained compositionally layered (~100  $\mu\text{m}$ ) granitic gneiss originating from the Swiss Alps in Northern Italy (Zurbriggen et al., 1998). The layer used is relatively homogenous, containing plagioclase (53 vol%), quartz (29 vol%), potassium feldspar (10 vol%), biotite (7 vol%) and accessory garnet/Fe- Ti oxides (1 vol%). Biotite and quartz are isolated within a feldspar framework (Fig. 2). The foliation is defined by aligned biotite grains and the elongation of other phases. Within the plane of the stretching lineation, plagioclase, quartz, potassium feldspar, and biotite have aspect ratios of 2.0, 1.8, 2.5, and 6.1, respectively, with the long axes parallel to the foliation. Average grain sizes of plagioclase, quartz, potassium feldspar, and biotite are 110, 75, 68, and 40  $\mu\text{m}$ , respectively. The grain sizes and aspect ratios were determined via analysis of SEM images of the undeformed starting material, using Image J. A LPO is present in quartz in which the  $\langle c \rangle$  axes are aligned, forming a girdle about the stretching lineation (Handy, 1986), which likely results in the  $\langle a \rangle$  axes ( $11\bar{2}0$ ) being subparallel with the direction of the stretching lineation (Fig. 3). The Gneiss Minuti has also been shown to have a magnetic anisotropy, which is likely due to shape anisotropy of magnetic accessory minerals (App. C).

One experiment was also performed on the Enfield Aplite, a fine grained granitic aplite, to more precisely determine the pressure conditions at faulting. Dell'Angelo and

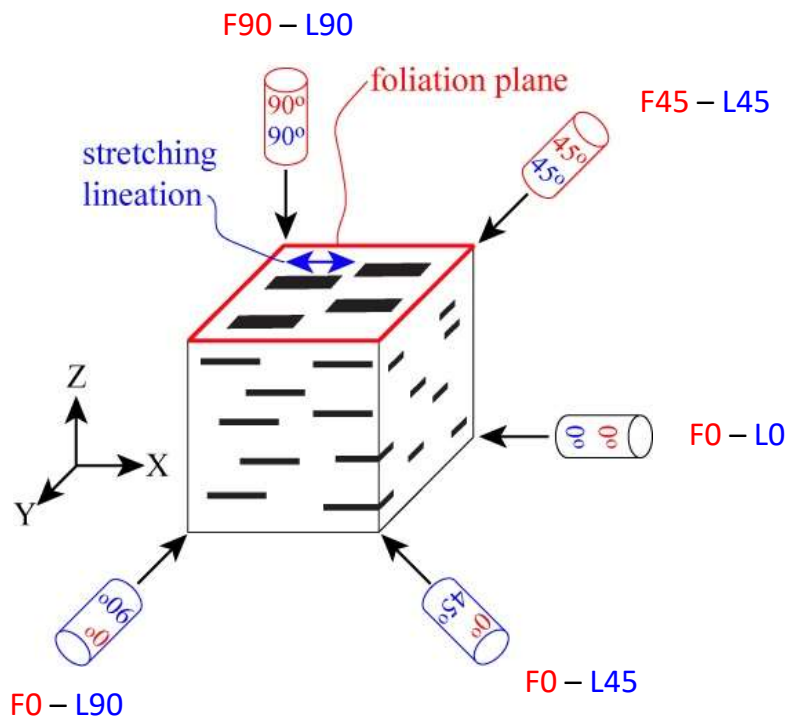


Figure 1. Schematic of Gneiss Minuti showing foliation and lineation. Orientations of cores collected for experiments in this study. Z, X, and Y coordinates indicate the directions of maximum shortening, maximum elongation, and intermediate elongation of the Gneiss Minuti, respectively.

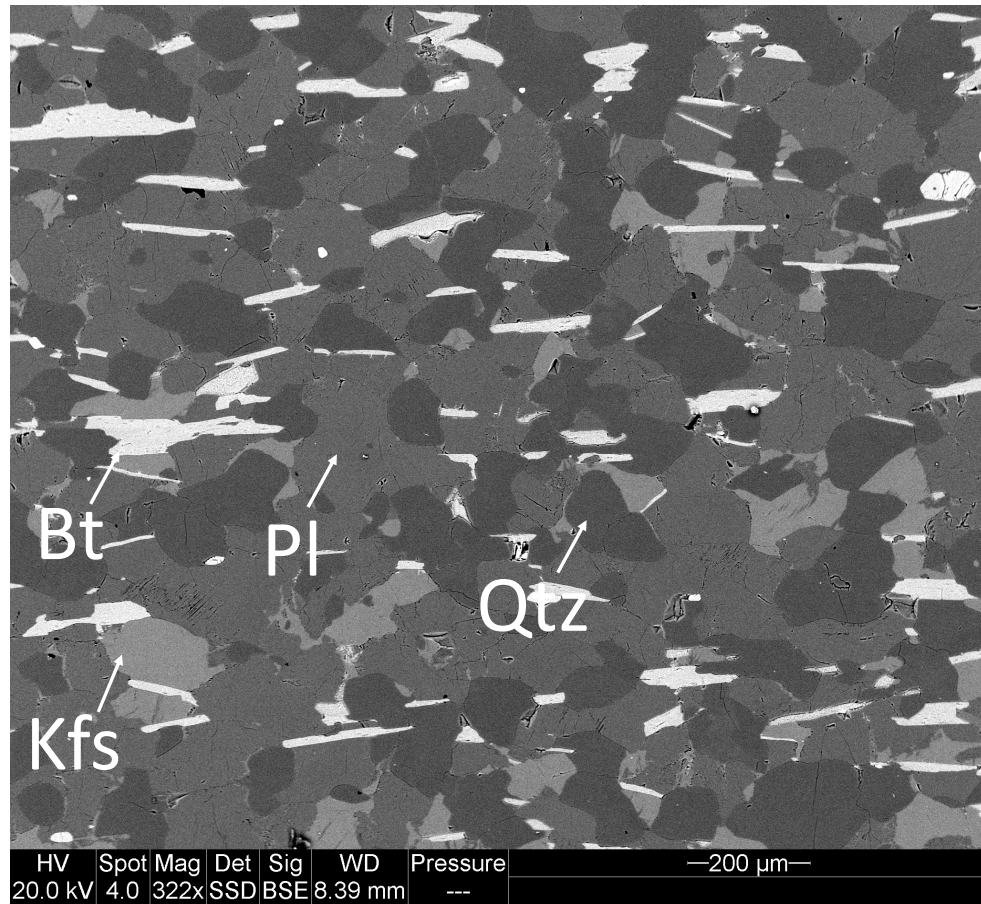


Figure 2. Gneiss Minuti starting material. The Gneiss Minuti layer used in all experiments has isolated biotite grains in a feldspar framework. This layer is composed of plagioclase (Pl, 53%), quartz (Qtz, 29%), potassium feldspar (Kfs, 10%), biotite (Bt, 7%). In SEM images of the Gneiss Minuti, quartz grains are the darkest gray, plagioclase grains are lighter gray, and potassium feldspar is the lightest gray. Biotite grains are elongate and near white, and the equant white grains are Fe/Ti oxides.

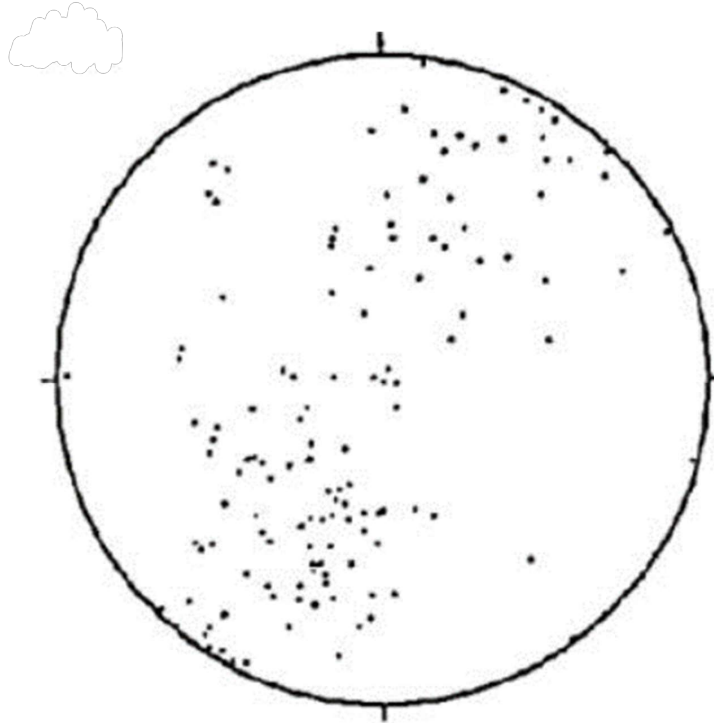


Figure 3. Quartz lattice preferred orientation (LPO) in the Gneiss Minuti. Lower hemisphere pole diagram of quartz  $\langle c \rangle$  axes with the foliation plane horizontal and the lineation East/West, plotted by Handy, (1986). This analysis was not performed on the layer of Gneiss Minuti used on this study, but it is likely that the layer used in this study has a similar quartz LPO, which would likely result in the  $\langle a \rangle$  axes being aligned sub-parallel with the stretching lineation, which is East/West on the stereonet plot.

Tullis (1988) performed an experimental deformation study using the Enfield Aplite, and characterized its composition as 30% quartz, 40% microcline, 27% oligoclase, and 3% biotite/magnetite, with an average grain size of 150  $\mu\text{m}$ .

## 2.2. Sample assembly and apparatus

Samples were cut to length using an Isomet saw and the cylinder faces were ground square to within a tolerance of  $<0.03\text{mm}$ . Samples were sealed in an inner jacket (Ag) and outer jacket (Ag) in order to chemically isolate the core from the NaCl confining medium. Samples were deformed as-is; they were not oven dried and no water was added prior to jacketing. Small  $\text{Al}_2\text{O}_3$  pistons ( $\sim 2.5 \times 5\text{mm}$ ) were included with the sample within the jacket to facilitate shear zone development (Fig. 4). Samples were deformed in a uniaxial compression geometry in a Griggs - type piston deformation apparatus (Griggs apparatus) using NaCl as the confining medium and a graphite furnace to apply heat (Fig. 4). A type K thermocouple placed within the assembly near the center of each sample was used to measure the temperature of the sample during deformation.

## 2.3 Experimental conditions

Cores were deformed brittlely at room temperature and  $\sim 50 - 150\text{ MPa}$  of confining pressure. This deformation occurred before the advancement of the load column. When the load column is advanced through the top Pb piece, the core is not loaded until the load column makes contact with the upper alumina piston and axial compression begins (Fig. 4). This point of contact is the hit point. Deformation that occurs before advancing the load column is referred to as pre-hit deformation. Strain was accommodated by forming

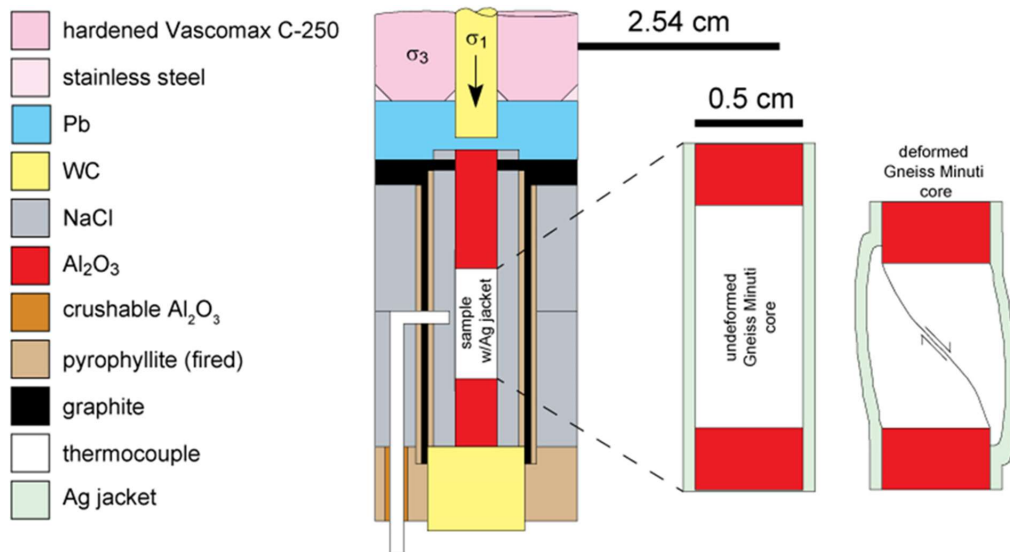


Figure 4. Schematic of sample assembly used in all experiments. Blow up of the sample shows the smaller Al<sub>2</sub>O<sub>3</sub> pistons, placed within the sample jacket to allow for the evolution of the fault/shear zone.

a through-going fault and resulted in ~6 – 10% shortening of each sample. Cores were then deformed in an axial compression geometry in the Griggs apparatus at a strain rate of  $\sim 2 \times 10^{-7} \text{ s}^{-1}$ ,  $P_c = 1500 \text{ MPa}$ , and  $T = 700^\circ\text{C}$ . These conditions were chosen to allow for the activation of crystal plastic deformation mechanisms in all phases while avoiding metamorphic reactions. Cores were brought to final conditions following a standard procedure beginning with the increase of confining pressure to 250 MPa over the period of 1 hour at  $\sim 25^\circ\text{C}$ . At this point, the temperature was increased to  $45^\circ\text{C}$ , then the pressure was increased to 300 MPa over the next 15 minutes. The pressure was then increased in 100 MPa increments every 15 minutes until reaching 1350 MPa. The temperature was increased to 100, 200, and  $300^\circ\text{C}$  at 300, 400 and 500 MPa, respectively. After reaching 1350 MPa, the temperature was increased from  $300^\circ\text{C}$  to the final temperature of  $700^\circ\text{C}$ . After reaching final pressure and temperature conditions, the load column of the apparatus was advanced at a constant displacement rate until the desired sample strain was obtained. When deformation was complete, the samples were quenched at a rate of  $200^\circ\text{C}/\text{minute}$  until reaching  $300^\circ\text{C}$  in order to preserve the deformational microstructures.

## 2.4 Mechanical data and sample analysis

Volt outputs of the apparatus transducers were recorded at a rate of 1 Hz throughout each experiment and were converted into values of displacement and calculated stress in relation to the dimensions of the sample. Stress values were corrected for change in loaded area by assuming a constant sample volume and the maintenance of a right cylinder form during shortening. The force of friction of the load column during compression was removed from the total force on the cylinder (Holyoke and Kronenberg, 2010). To obtain strain values, the hit point is calculated by analyzing the run-in curve.

This consists of an initial linear increase in load as the  $\sigma_1$  piston advances through the top Pb piece within the sample assembly. As the  $\sigma_1$  piston makes contact with the sample, the load curves up into a steeper linear increase in load, which represents elastic deformation. The hit point is found at the intersection of the two linear portions of the run-in curve.

After being quenched and returned to room temperature and pressure, samples were cut in half parallel to the long axis of the sample and perpendicular to the shear plane of the fault. A doubly polished thin section was prepared from one sample half of each experiment and used to conduct microstructural analysis with a standard petrographic microscope and a scanning electron microscope with a backscatter diffraction detector (SEM-BSE).

## CHAPTER III

### RESULTS

A total of 10 experiments were conducted in order to observe the different stages of shear zone formation (Table 1). All samples were pre-faulted during the process of pressurization. The majority of axial strain induced during the process of pressurization occurs at  $\sim 25^{\circ}\text{C}$ , between the pressures of  $\sim 50\text{-}150\text{ MPa}$ . The total axial strain caused by the pre-faulting process was  $\sim 6\text{-}11\%$  in each sample (Table 2). Pre-hit strain was obtained for each sample using two different methods that produce similar values: 1) sample lengths were measured after deformation and compared with the value of strain calculated from the Griggs deformation cycle, and 2) displacement hit points were calculated by analyzing the run-in curve and compared with hit point estimation which can be obtained using the dimensions of the load column and original sample length.

Three hydrostatic experiments were conducted to characterize the microstructures in the fault before and after being annealed for seven days at  $700^{\circ}\text{C}$ . In two of these experiments, the samples were pressurized, pre-faulted, and brought to final conditions following the standard procedure, but they were not subjected to any axial strain after reaching the final temperature of  $700^{\circ}\text{C}$ . A third hydrostatic experiment was pressurized to only  $300\text{ MPa}$  with no added temperature in order to more precisely determine when the faulting occurs.

Two experiments were deformed until they yielded in order to characterize low strain microstructures. Five experiments were conducted on cores of varying foliation orientations and strained to peak stress in order to determine the strengths in relation

Table 1. Orientation, strain, and peak stress (where applicable) for all experiments. All experiments were brought to a temperature of 700°C, a confining pressure ( $P_c$ ) of 1500 MPa, and when subjected to axial loading, a constant strain rate of  $\sim 2 \times 10^{-7} \text{ s}^{-1}$ .

Experiment	Orientation	Applied Strain (%)	Peak Stress (MPa)	Time at conditions (hr)
Z-148	F0-L45	15.43	1110	504
Z-150	F0-L45	14.01	1040	453
Z-151	F90-L90	15.51	930	498
Z-152	F0-L0	15.36	1210	471
Z-153	F0-L90	13.49	1010	427
Z-154	F0-L0	2.87	560	240
Z-155	F0-L45	2.17	480	221
Z-156	F0-L45	Hydrostatic	-	1
Z-157	F0-L45	Hydrostatic	-	166
Z-159	F0-L45	44.03	1110	855

Table 2. Strain and pre-hit deformation data, obtained from deformation cycle calculations, sample measurements, and hit point calculations.

Experiment	Sample Length (mm)		Strain (%)		Pre - Hit Deformation (%)	
	Initial	Final	Calculated from deformation cycle	Measured from sample length	From calculated hit point	Measured sample strain - strain from deformation cycle
Z-148	10.15	7.92	15.4	22.0	8.9	6.5
Z-150	10.12	7.99	14.0	21.0	7.5	7.0
Z-151	10.18	8.08	15.5	20.7	7.0	5.1
Z-152	10.11	8.12	15.4	19.7	7.6	4.3
Z-153	10.43	8.14	13.5	21.9	8.1	8.4
Z-154	10.22	9.04	2.9	11.5	7.1	8.6
Z-155	10.03	8.84	2.2	11.9	7.6	9.7
Z-156	10.17	9.58	N.L.A. <sup>1</sup>	5.9	-	5.9
Z-157	10.05	8.90	N.L.A.	11.4	-	11.4
Z-159	10.12	4.57	44.0	54.8	10.5	10.8
Z-163	12.76	12.54	N.L.A.	1.7	-	1.7

1: N.L.A = no load applied.

to the foliation orientation and characterize the microstructures at peak stress. One sample was strained to 44% to determine the degree of strain weakening as the fault microstructure evolved to a steady state of stress.

### 3.1. Mechanical data

All samples were strained 6 - 11% during pressurization (i.e., pre-faulted). Deformation experiments were then strained by axial compression to further strains of ~2 - 45% (Table 2). Unless otherwise specified, values of strain in this section refer to the applied axial strain at final conditions, and do not include strain caused by pre-faulting. The two low strain experiments yielded between 1 - 2% strain ( $\epsilon$ ) at a differential stress ( $\sigma$ ) of ~450 MPa and were quenched shortly after yielding (Fig. 5). The six experiments deformed to peak stress all have similar mechanical behavior (Fig. 6). Differential stresses increase linearly until yielding at  $\sigma = \sim 1 - 2\%$  and continue to increase until reaching a peak differential stress of ~900 to 1200 MPa at a strain of ~12 - 15%. The core that had the lowest peak stress was oriented with the foliation perpendicular to  $\sigma_1$  (F90-L90;  $\sigma = \sim 930$  MPa), and the core with the greatest peak stress was oriented with the foliation parallel to  $\sigma_1$  cored within the plane containing the stretching lineation (F0-L0;  $\sigma = \sim 1210$  MPa) (Fig. 6, Table 1). The high strain sample underwent strain weakening until ~40%, where it deformed at a constant stress of ~600MPa.

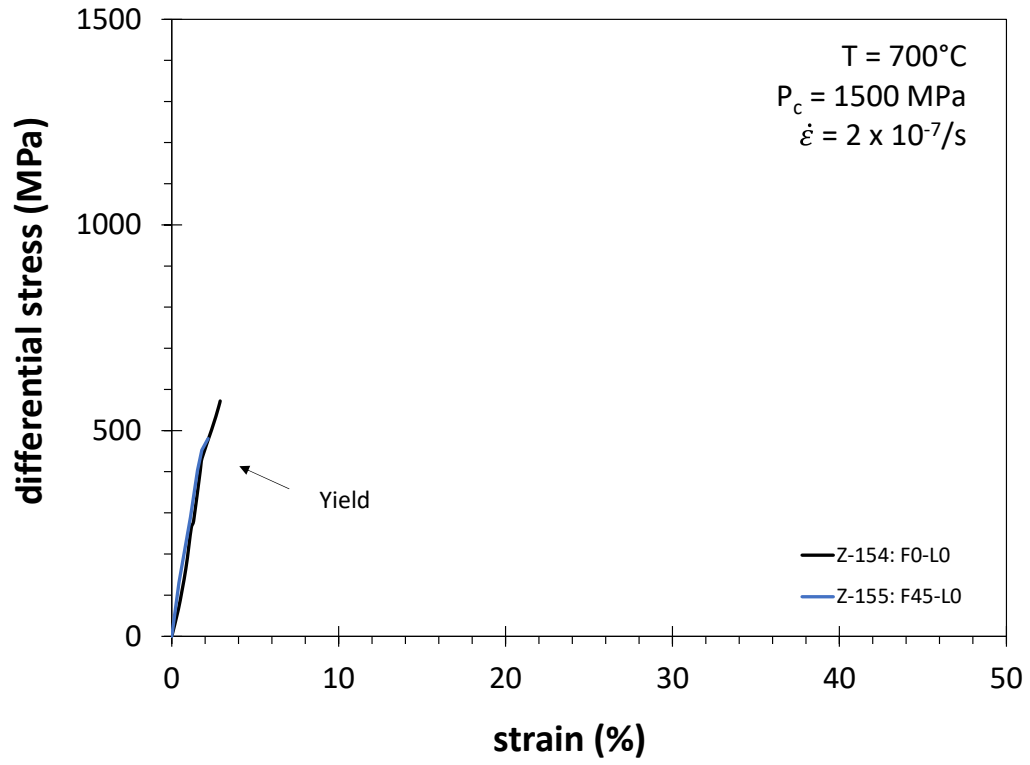


Figure 5. Low strain mechanical data. Two experiments were stopped soon after reaching the yield point at a strain of  $\sim 2\%$ .

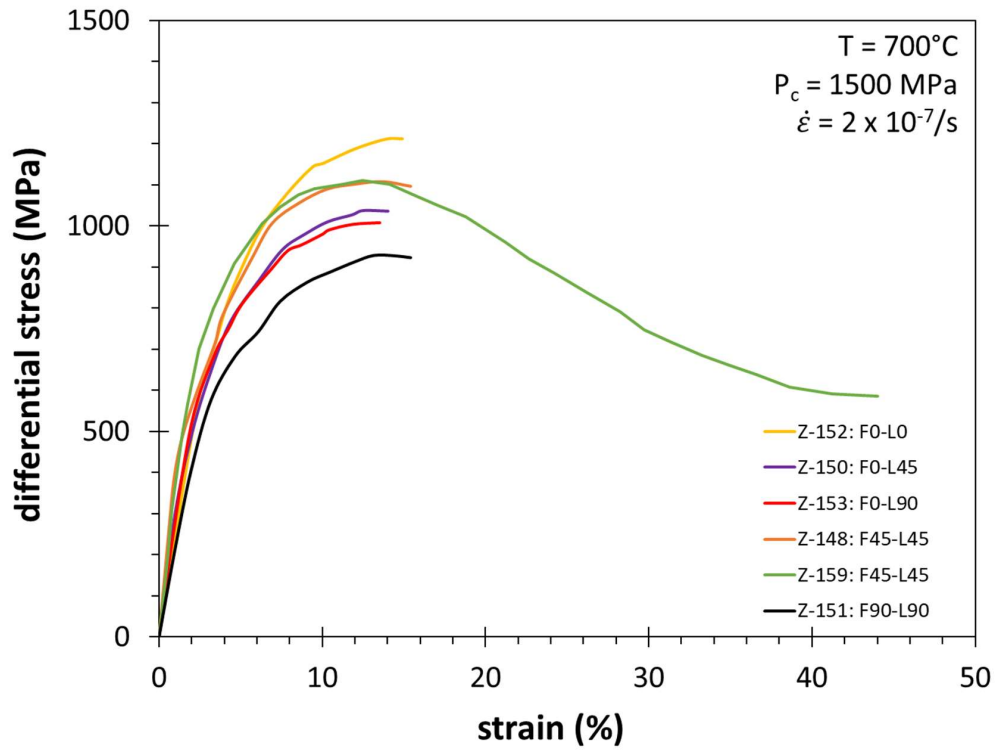


Figure 6. Intermediate and high strain experiments mechanical data. Peak differential stresses range from ~950 – 1200MPa, and the high strain experiment strain weakened to what appeared to be a steady state stress of ~600MPa, at ~44% applied axial strain.

## 3.2. Microstructures

### 3.2.1. Hydrostatic

Three hydrostatic experiments were not subjected to axial loading by advancing the load column of the Griggs apparatus, but all of them contained through going faults, which formed during pressurization.

#### 3.2.1.1. Low-pressure hydrostatic

I performed a low-pressure hydrostatic experiment on a core of the Enfield Aplite ( $P_c = 250$  MPa), in order to determine when the faulting of all samples occurred. The sample contains a through-going fault zone which cross-cuts the otherwise undeformed host rock. The fault zone is porous and contains variably-sized angular grains ranging from larger porphyroclasts  $>100$   $\mu\text{m}$  to very fine-grained material in the sub-micron scale (Fig. 7). The faulting is likely caused by stress concentrations on the faces of the rock cores as a result of axis loading due to a deformed base plate. At low pressure, the stress concentration is sufficient to induce microcracking in feldspars and possibly quartz.

#### 3.2.1.2. Short hydrostatic

The short hydrostatic experiment ( $t = 1$  hr) was performed on a core with the foliation and lineation in the F45 - L45 orientation. A through-going fault sub-parallel with the foliation plane cross-cuts the undeformed host rock, forming a sharp boundary (Fig. 8a, 8b). The fault zone is composed of angular and variably sized grains, ranging from sub micron scale to  $\sim 10$   $\mu\text{m}$  (Fig. 8c). Larger grains of feldspar within or near to the fault sometimes have a patchy undulatory extinction. The fault zone average thickness is  $\sim 100$   $\mu\text{m}$  in width but thickness is variable; the thickness is  $\sim 200$   $\mu\text{m}$  near the center of the

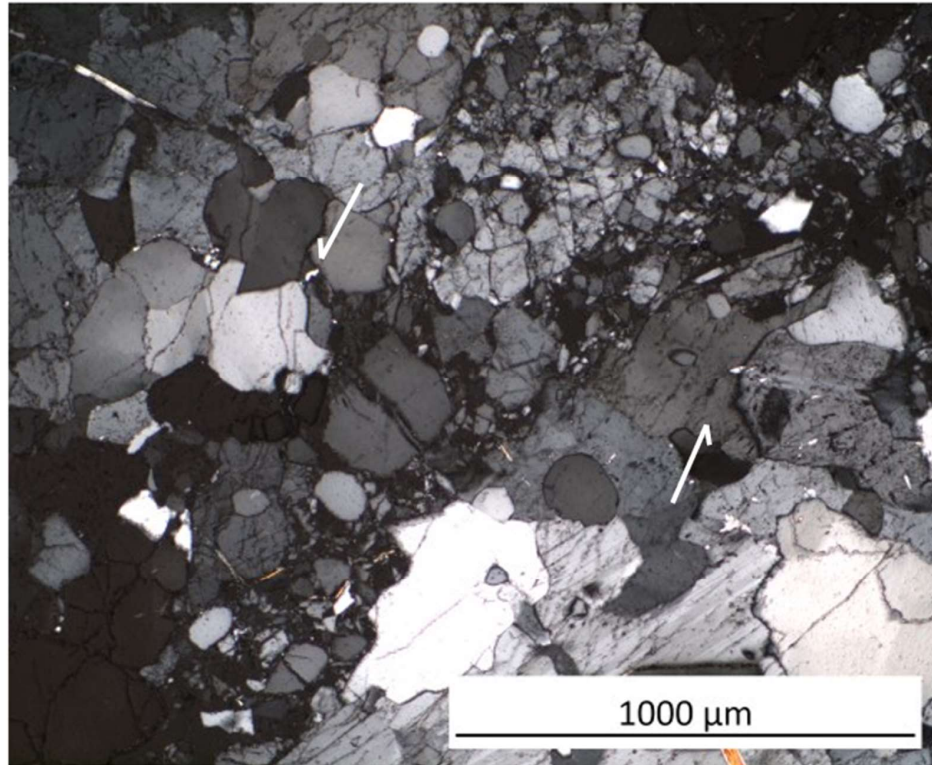


Figure 7. Fault in Enfield Aplite. Enfield Aplite sample was pressurized to 300 MPa. A through-going fault composed of fine grained angular grains cross-cuts the sample.

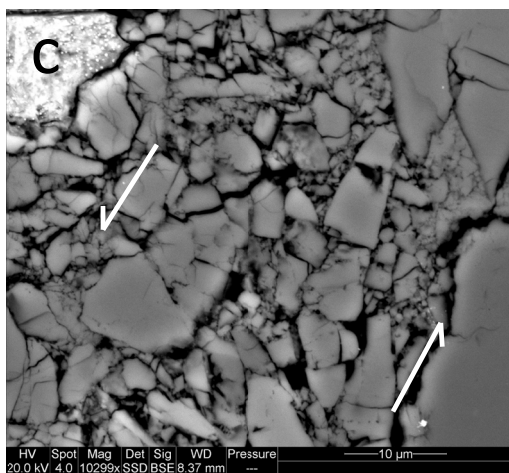
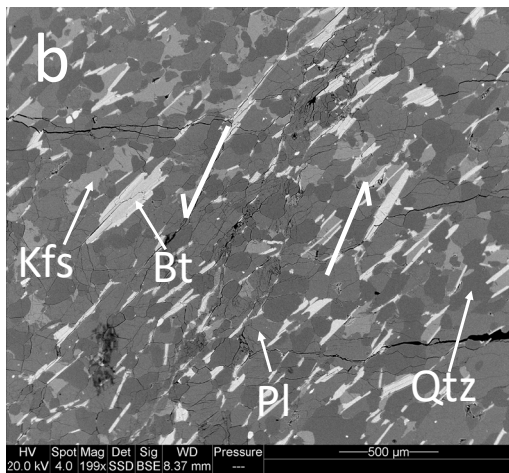
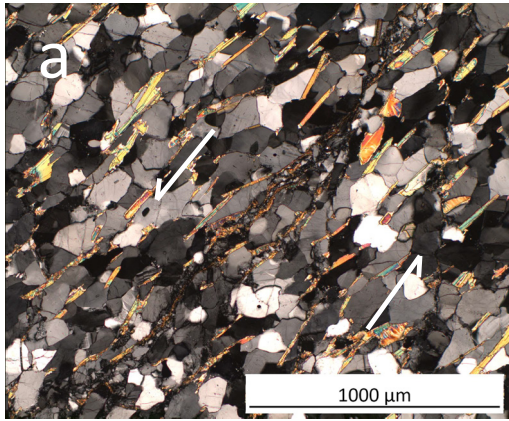


Figure 8. Short hydrostatic experiment.  $T = 700^{\circ}\text{C}$ ,  $P_c = 1500 \text{ MPa}$ ,  $t = 1 \text{ hour}$ . a) optical micrograph showing brittle fault in short hydrostatic experiment. b) SEM image of brittle fault. c) SEM high magnification image of fault gouge, displaying angular grains and porosity. In all images, the orientation of  $\sigma_1$  is vertical.

sample and  $<10\ \mu\text{m}$  near the pistons. Near the ends of the sample, some areas of the fault are only identifiable by the presence deformed biotite and/or displaced grains.

### 3.2.1.3. Long hydrostatic

The long hydrostatic experiment ( $t = 166\ \text{hr}$ ) was also performed on a core with the foliation and lineation in the F45 - L45 orientation. A through-going fault cross-cuts the core and the foliation of the undeformed host rock and forms a sharp boundary (Fig. 9a, 9b). The through-going fault is composed of finely recrystallized material, contains little to no porosity, and grains are rounded and interlocking (Fig. 9e, f). Finely recrystallized monophase domains that appear to be deformed singular grains dominate the shear zone. However, there are some areas of phase mixing present in this sample, generally at the boundaries between monophase domains (Fig. 9c).

### 3.2.2. Low strain experiments

Two cores were deformed to low strains and quenched shortly after yielding: one core in the orientation F0-L0, and one in the orientation F45-L45 (Table 1). Both samples contain a through-going shear zone which cross cuts the undeformed host rock (Fig. 10a). The shear zones are composed of zones of finely recrystallized material, with rare angular grains and little to no porosity (Fig. 10a, 10b). The recrystallized grain size is difficult to determine; at the scale of a petrographic microscope and SEM, the grain boundaries of finely recrystallized zones are not visible. Single domain zones that are likely to represent areas of recrystallized fine-grained material have the appearance of being single deformed grains when viewed through the SEM (Fig. 10b, 10c). The microstructures observed in the low strain experiments are similar to those observed in the long hydrostatic sample. While the shear zone is dominated by areas of finely recrystallized monophase material, areas of mixed phases are also present (Fig. 10c).

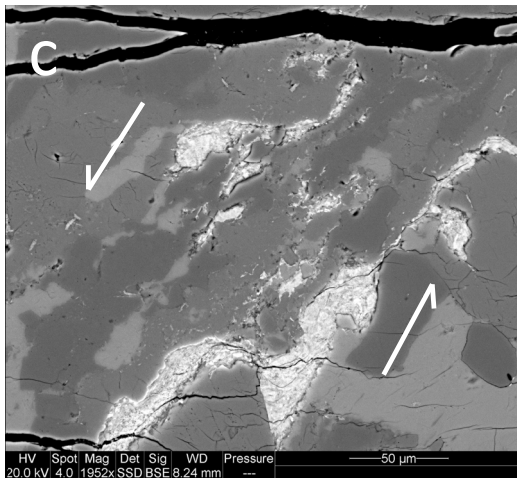
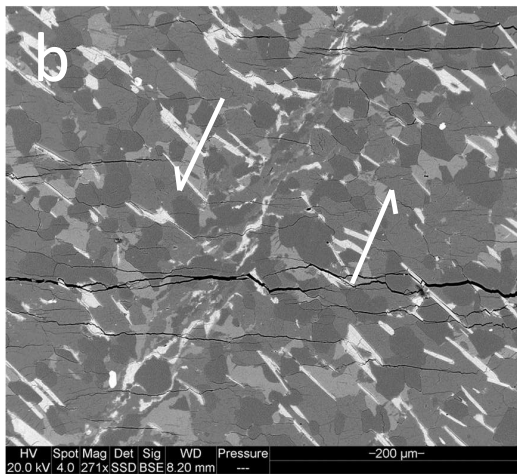
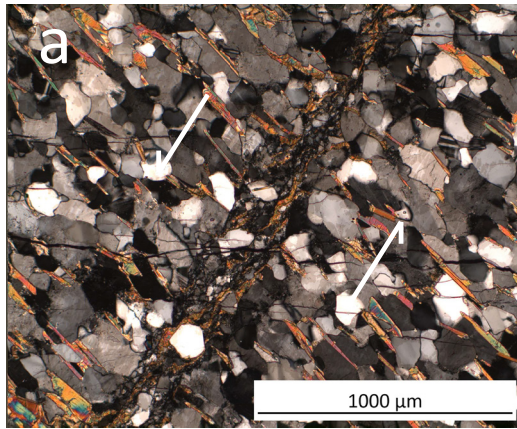


Figure 9. Long hydrostatic experiment.  $T = 700^{\circ}\text{C}$ ,  $P_c = 1500 \text{ MPa}$ ,  $t = 7 \text{ days}$ . a) Optical micrograph showing annealed fault. b) SEM image of annealed fault, in the same location as in 9a (note quartz porphyroclast in the lower left shear zone). c) High magnification SEM image of annealed zone in the long hydrostatic sample. Comparison of optical and SEM imaging reveals that what appears to be single grains in SEM images are actually zones of finely recrystallized material. In all images, the orientation of  $\sigma_1$  is vertical.

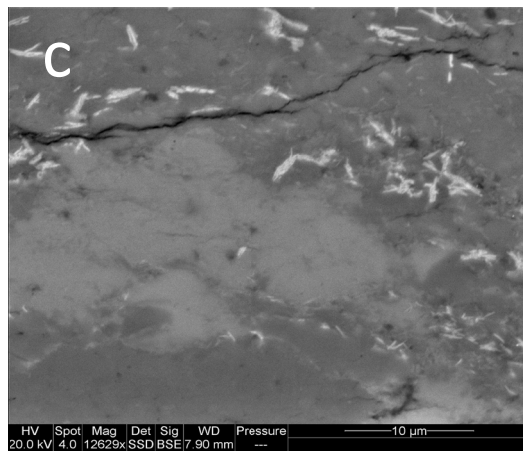
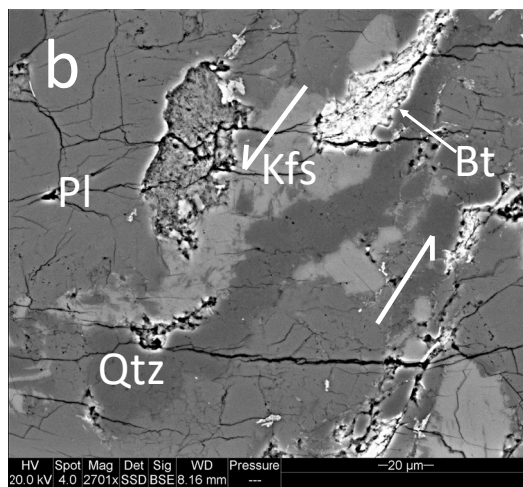
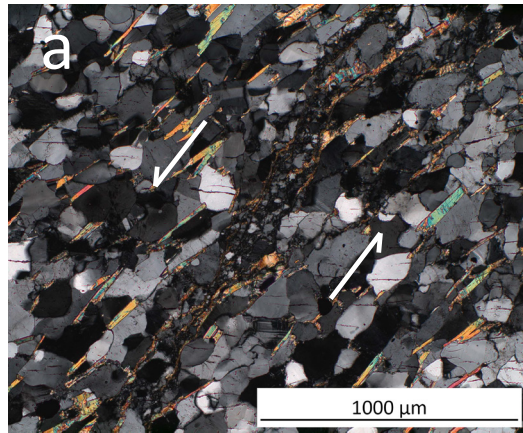


Figure 10. Low strain experiments.  $T = 700^\circ$ ,  $P_c = 1500 \text{ MPa}$ ,  $\epsilon = \sim 2 \times 10^{-7}$ . a) optical micrograph of low strain shear zone. b) SEM image of recrystallized quartz and feldspar. c) SEM image showing recrystallized mixed phases. In all images, the orientation of  $\sigma_1$  is vertical.

### 3.2.3. Intermediate strain experiments

One core in each of the five orientations was deformed until it reached a peak differential stress (Table 1, Fig. 1). All samples contain a through-going fine-grained shear zone which cross cuts undeformed host rock. The shear zone in the sample with the foliation at  $45^\circ$  cross cuts the foliation. In all samples, the shear zones form a relatively sharp boundary with the host rock (Fig. 11a). The shear zones are composed of zones of mixed quartz and feldspar as well as single phase zones of finely recrystallized grains (Fig 11b, 11c). Biotite grains are kinked and recrystallized. Larger quartz porphyroclasts within the shear zones often display undulatory extinction and deformation lamellae.

### 3.2.4. High strain experiment

One core with the foliation and lineation in the F45 - L45 orientation was deformed to high strain ( $\epsilon = 44\%$ ). A through-going, fine-grained shear zone cross-cuts the foliation in the host rock, and the host rock adjacent to the shear zone is deformed (Fig 12a, b, c); (Fig. 13a, b). Within the shear zone there are layers of monophasic domains, however there is a greater presence of mixed phase domains compared with lower strain samples. The mixed phase domains are highly sheared, containing fine-grained recrystallized recrystallized assemblages of feldspar, quartz, and biotite (Fig. 13c). The areas adjacent to the shear zone appear to have been deformed by a mixture of crystal plastic and brittle deformation mechanisms. Many quartz grains have been flattened and have undulatory extinction and deformation lamellae (Fig. 13b). Some feldspar grains adjacent to the shear zone have been fractured, forming bookshelf faults, and fractures appear to be filled with recrystallized grains (Fig. 13c). Grain boundaries in the host rock near to the shear zone are sometimes surrounded by deformed biotite or fine-grained material which could be recrystallized feldspar and/or quartz.

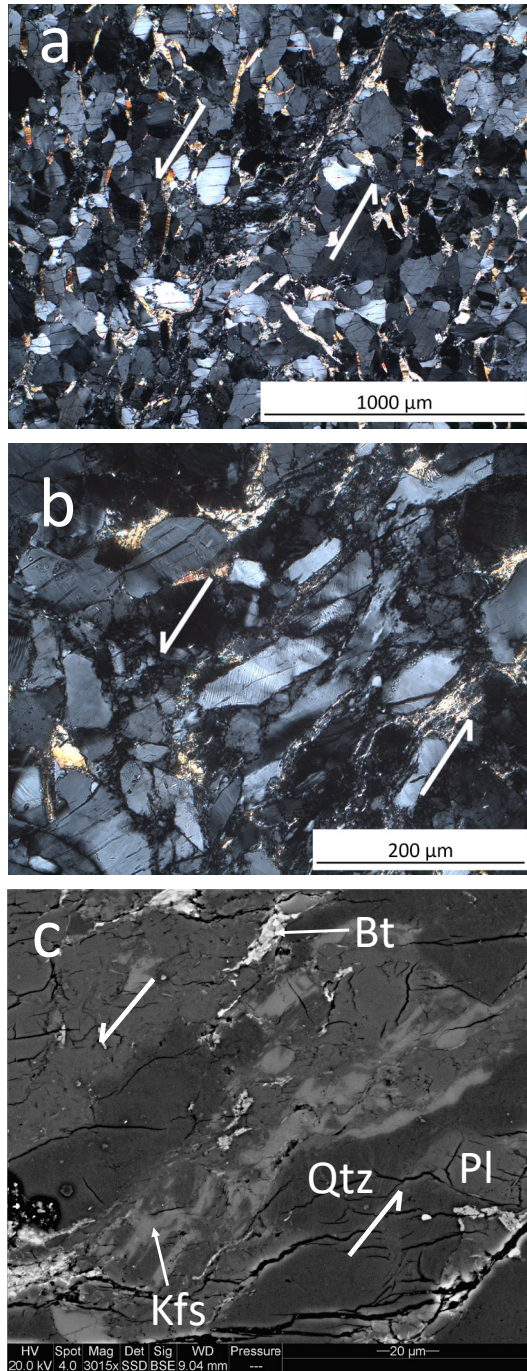


Figure 11. Intermediate strain experiments. Samples were strained to their peak stress.  $T = 700^\circ\text{C}$ ,  $P = 1500\text{ MPa}$ ,  $\dot{\epsilon} = \sim 2 \times 10^{-7}\text{ s}^{-1}$ . a) ( $T = 700^\circ\text{C}$ ,  $P = 1500\text{ MPa}$ ,  $\dot{\epsilon} = \sim 2 \times 10^{-7}\text{ s}^{-1}$ ,  $\epsilon = 14\%$ ) Optical micrograph of shear zone. b) ( $T = 700^\circ\text{C}$ ,  $P = 1500\text{ MPa}$ ,  $\dot{\epsilon} = \sim 2 \times 10^{-7}\text{ s}^{-1}$ ,  $\epsilon = 14\%$ ) Optical micrograph, attenuated quartz grain displays deformation lamellae and undulatory extinction. c) ( $T = 700^\circ\text{C}$ ,  $P = 1500\text{ MPa}$ ,  $\dot{\epsilon} = \sim 2 \times 10^{-7}\text{ s}^{-1}$ ,  $\epsilon = 15\%$ ) SEM image showing mixed phases. In all images, the orientation of  $\sigma_1$  is vertical.

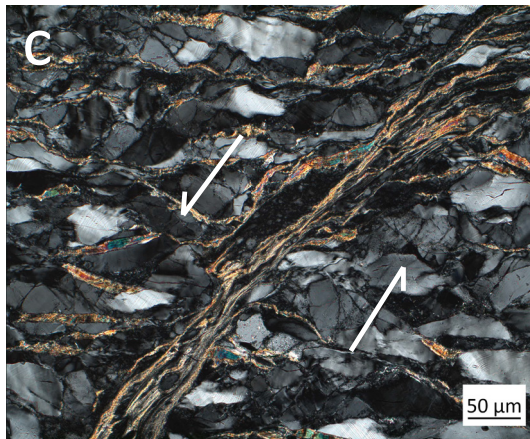
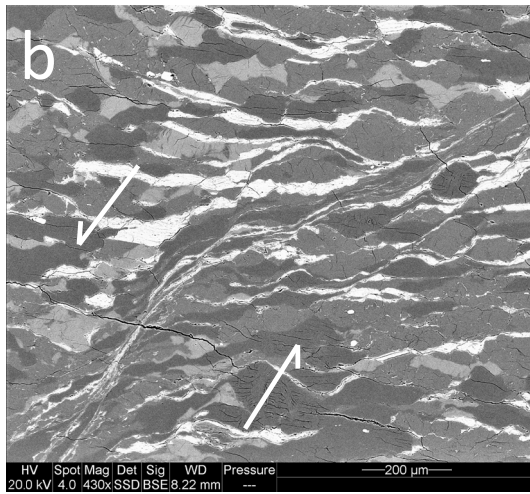
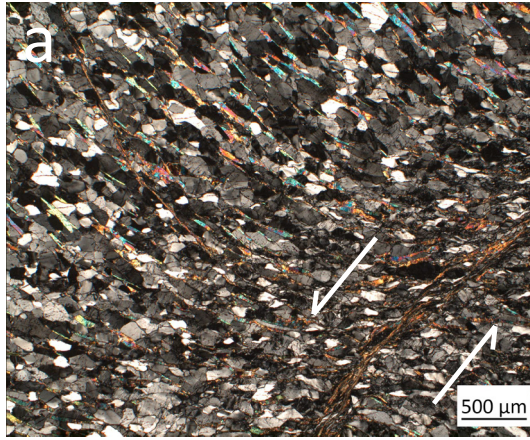


Figure 12. Lower magnification images of the highly strained sample.  $T = 700^{\circ}\text{C}$ ,  $P = 1500\text{ MPa}$ ,  $\dot{\epsilon} = \sim 2 \times 10^{-7}\text{ s}^{-1}$ ,  $\epsilon = 44\%$  a) Foliation is deflected  $\sim 45^{\circ}$  into the shear zone. b) Phases within the shear zone are highly attenuated / recrystallized. Near the shear zone, grains are deformed, showing flattening, undulatory extinction, and deformation lamellae. c) Evidence of brittle deformation of feldspars is present outside of the main shear zone; feldspar grains display bookshelf faulting. In all images, the orientation of  $\sigma_1$  is vertical.

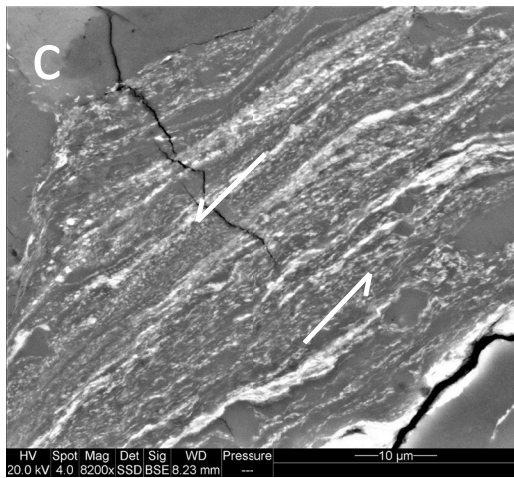
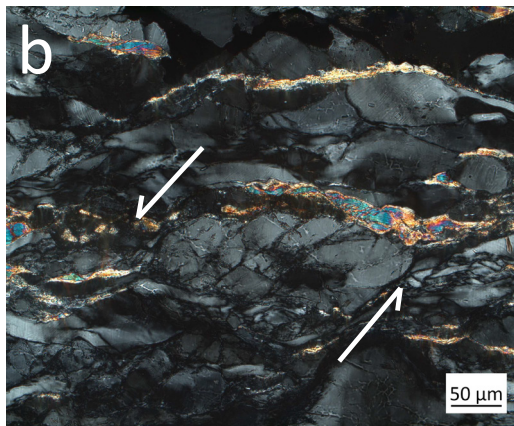
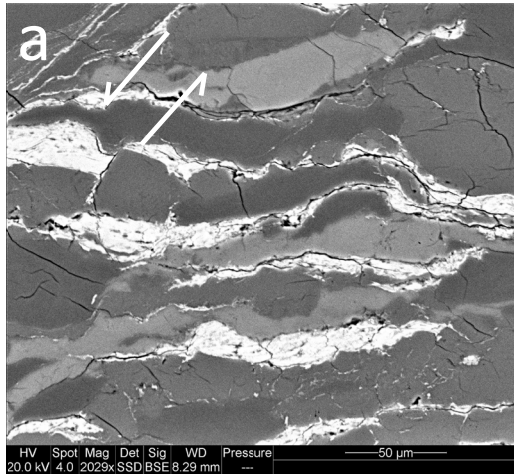


Figure 13. Higher magnification images of the highly strained sample.  $T = 700^{\circ}\text{C}$ ,  $P = 1500\text{ MPa}$ ,  $\dot{\epsilon} = \sim 2 \times 10^{-7}\text{ s}^{-1}$ ,  $\epsilon = 44\%$ <sup>c</sup> a) SEM image showing attenuated grains within and near to the shear zone. b) slightly away from the shear zone, grains appear to be homogeneously flattened. c) Fine grained mixed phases are present within the shear zone. In all images, the orientation of  $\sigma_1$  is vertical.

## CHAPTER IV

### DISCUSSION

All samples developed a pre-existing fault during pressurization and subsequently developed a ductile shear zone when the strain imposed by the advancement of the load column localized along the fault. In samples strained to  $\epsilon \leq 15\%$ , strain localized along the pre-existing fault and was accommodated by crystal plastic deformation mechanisms. The microstructures found in the brittle pre-fault were overprinted by this later crystal plastic deformation. Sample strength at peak stress was somewhat variable but does not appear to have a direct relationship with foliation / lineation orientation (Fig. 14). At higher strains, the rock surrounding the ductile shear zone also begins to accommodate strain.

#### 4.1. Deformation mechanisms

Microstructures in the series of experiments performed in this study evolve as the deformation mechanisms change. The short hydrostatic experiment includes angular grains with a highly variable grain size and significant porosity. These microstructures are consistent with brittle mechanisms and are expected at the conditions that the fault formed ( $T = \sim 25^\circ \text{C}$ ,  $P_c = 50 - 150 \text{ MPa}$ ). Tullis and Yund (1977) deformed the Westerly Granite at similar conditions and observed that both quartz and feldspar deformed by microfractures with little to no dislocations present; microstructures that are consistent with those observed in my experiments. The fault gouge formed by cataclasis appears to

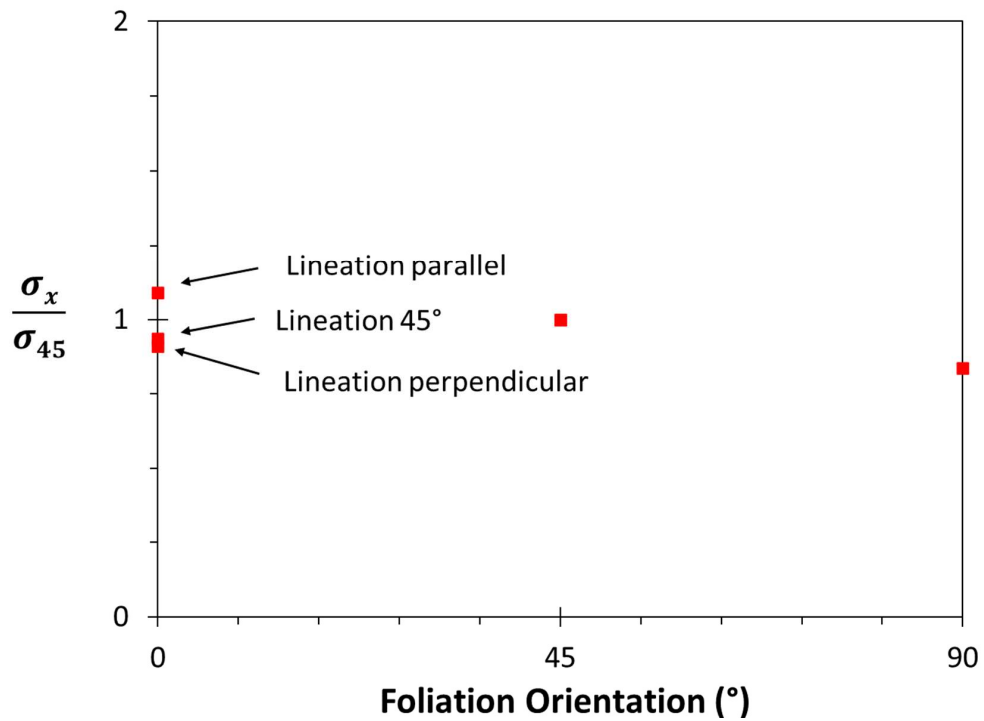


Figure 14. Peak differential stresses vs. orientation. The six experiments that reached a peak stress, in respect to the angle of the foliation to the direction of compression ( $\sigma_1$ ) and normalized to strength of the cores deformed at 45° to the foliation. The two experiments taken to peak stress in with the foliation at 45° have nearly identical strengths (~1100MPa). The peak stresses do not demonstrate a predictable relationship with their orientation relative to the foliation and lineation of the Gneiss Minuti.

be feldspar rich (Fig. 9c). Feldspar is more likely to experience fracturing and reduction in grain size by cataclasis than quartz because of the two directions of cleavage that feldspars contain. This observation is similar to the observations of Tullis and Yund (1977) who performed TEM analysis on experimentally produced brittle faults in samples of the Westerly Granite. They found that the resulting faults in the Westerly Granite tended to preferentially avoid quartz grains, and the gouge consisted largely of feldspar.

In contrast to the short hydrostatic sample ( $t = 1$  hr), the long hydrostatic sample ( $t = 166$  hr) displays little evidence of brittle deformation. The geometry of the through-going fault is similar but in the long hydrostatic sample the grain boundaries are rounded and there is little to no porosity (Fig. 9c). These microstructures are due to hydrostatic annealing at final conditions ( $T = 700^{\circ}\text{C}$ ,  $P_c = 1500$  MPa) for the seven-day period. These microstructures likely represent those present in all experiments prior to being deformed by the advancement of the load column, which takes seven days to start loading the sample after starting to advance the load column through the top lead piece of the sample assembly.

The samples that were deformed to low strains and the long hydrostatic sample have identical microstructures (Fig. 10a, 10b, 10c). They both contain shear zones that are dominated by recrystallized monophase domains, but they also have some rare mixed phase domains. Mixed phases are often thought to be the result of grain boundary sliding in naturally occurring mylonites and ultramylonites (e.g. Stünitz and Fitzgerald, 1993; Fliervoet et al., 1997; Kilian et al., 2011) as well as in experimentally deformed materials (Barnhoorn et al., 2005; Cross and Skemer, 2017). However, in the case of the long hydrostatic experiment, no further strain was accommodated after the sample reached its final temperature and pressure ( $T = 700^{\circ}\text{C}$ ,  $P_c = 1500$  MPa). Thus, areas of mixed phases in the long hydrostatic sample are the result of cataclastic deformation and subsequent annealing. The mixed phase domains in the low strain samples are also likely due to

cataclastic deformation and annealing, since a very small amount of permanent strain was accommodated in these samples after they reached a yield point.

There are greater amounts of mixed phase domains in the samples deformed to their peak stress than in the samples deformed to low strains (Fig. 11c). An increase in phase mixing can be attributed to an increase in deformation by diffusion-accommodated grain boundary sliding, which is a grain size sensitive deformation mechanism (Kilian et al., 2011; Cross and Skemer, 2017). While a monophasic polycrystalline rock may undergo grain growth via grain boundary migration, the presence of a secondary phase can inhibit or stop grain growth (Evans et al., 2001). Fukuda et al. (2018) deformed fine-grained quartz aggregates that initially deformed by diffusion creep, but as the grain size increased the deformation mechanism changed to dislocation creep and the strength also increased. However, polyphase aggregates have been shown to behave differently: Cross and Skemer (2017) performed high strain shear experiments on poorly mixed calcite/anhydrite aggregates and observed that grain boundary sliding occurred as monophasic layers became increasingly thin, creating more polyphase contacts, and increased phase mixing. Barnhoorn et al. (2005) also deformed calcite/anhydrite aggregates and observed that phase mixing due to diffusion-accommodated grain boundary sliding resulted in strain weakening and strain localization. It is likely that diffusion-accommodated grain boundary sliding is the dominant mechanism within the shear zones in my samples. There is an increase in polyphase contacts with increasing strain, that prevents grain growth and promotes further deformation by diffusion-accommodated grain boundary sliding. Grain boundary sliding is active at low strains in some parts of the shear zones since some initial phase mixing occurred during the pre-faulting.

The host rock in all low strain and peak stress samples is relatively undeformed away from the shear zone (Fig. 11a). This observation indicates that the materials within the shear zone in these samples are weaker than the coarse-grained host rock and deform

by lower stress mechanisms. Larger porphyroclasts of quartz within the shear zones of samples strained to their peak stress often have undulatory extinction and deformation lamellae, microstructures consistent with dislocation creep. However, the dominant deformation mechanism within the shear zone is likely diffusion-accommodated grain boundary sliding in the mixed phase domains.

In the highly strained sample, mica grains are highly sheared within the shear zone (Fig. 12c). Higher magnification SEM images show that these areas consist of finely recrystallized biotite (Fig. 13c). In contrast with the samples from the low and intermediate strain experiments, the rock surrounding the shear zone appears to have accommodated a significant amount of the strain in this sample (Fig. 13b, 13c). Quartz grains have been flattened, have undulatory extinction and deformation lamellae, microstructures consistent with dislocation creep (Hirth and Tullis, 1992). Feldspar grains adjacent to the shear zone have been deformed by a combination of brittle and crystal plastic mechanisms. Some feldspar grains have series of fractures along which displacement has occurred, resulting in bookshelf faults (Fig. 13b), and finely recrystallized grains are observed within these fractures and at grain boundaries, consistent with microstructures observed in feldspar aggregates deformed by recrystallization-accommodated dislocation creep (Tullis and Yund, 1985). The transitional nature of feldspars outside of the shear zone is consistent with the results of Tullis and Yund (1985), which observed that feldspar aggregates deformed by a combination of brittle faulting and recrystallization accommodated dislocation creep at 700 – 850°C and  $\dot{\epsilon} = 10^{-6} \text{ s}^{-1}$ , conditions that are comparable to the deformational conditions of my experiments.

## 4.2. Shear strain analysis

Because the microstructures suggest that the majority of the strain in these experiments is accommodated along the shear zone, it is possible to estimate the total shear strain applied at final conditions by:

$$\Delta_a/\Delta_s = \cos(\theta) \quad (\text{Eq. 1})$$

where  $\Delta_a$  = axial displacement caused by advancement of the  $\sigma_1$  piston,  $\Delta_s$  = displacement along the shear zone and  $\theta$  = the angle of the shear zone to direction of  $\sigma_1$ . Total shear strain ( $\gamma$ ) is given by:

$$\gamma = \Delta_s/w_s \quad (\text{Eq. 2})$$

where  $w_s$  = average width along the shear zone. The shear strain rate is then calculated by applying the total amount of time elapsed from the yield point (when strain begins to be accommodated along the shear zone) to the time when the experiment is quenched (Table 3). The shear strain rate can then be converted to an equivalent axial strain rate after Paterson and Olgaard (2000) by:

$$\dot{\epsilon} = 1/\sqrt{3} \dot{\gamma} \quad (\text{Eq. 3})$$

where  $\dot{\gamma}$  is the shear strain rate and  $\dot{\epsilon}$  is the equivalent axial strain rate. These calculations indicate that the strain rate within the shear zone is generally about two orders of magnitude faster than the average axial strain rate (Table 3). These results are consistent with other experimental studies of strain localization. Holyoke and Tullis (2006) performed shear experiments on a layer of the Gneiss Minuti, which resulted in

Table 3. Shear strain calculations. Shear strain along localized zones of ductile deformation, calculated with the assumption that all strain was accommodated along the shear zones. The shear strain rate was found by dividing the total shear strain by the elapsed time from the yield point to the time of quenching. The equivalent axial strain rate is calculated as  $\dot{\epsilon} = 1/\sqrt{3} \cdot \dot{\gamma}$  where  $\dot{\gamma}$  is the shear strain rate and  $\dot{\epsilon}$  is the equivalent axial strain rate (Paterson and Olgaard, 2000).

Experiment	Applied axial Strain Rate ( $s^{-1}$ )	Sample Length (mm)	Shear Zone Angle ( $^{\circ}$ )	Shear Zone Average Width ( $\mu m$ )	Applied Strain (%)	Axial Displacement (mm)	Shear Zone Displacement (mm)	Shear Strain	Elapsed Time (s)	Shear strain rate ( $s^{-1}$ )
Z-148	$\sim 2 \times 10^{-7}$	10.15	29	58	15.43	1.57	1.79	30.86	927580	$3.33 \times 10^{-5}$
Z-150	$\sim 2 \times 10^{-7}$	10.12	32	100	14.01	1.42	1.67	16.71	857505	$1.95 \times 10^{-5}$
Z-151	$\sim 2 \times 10^{-7}$	10.18	26	87	15.51	1.58	1.76	20.20	942932	$2.14 \times 10^{-5}$
Z-152	$\sim 2 \times 10^{-7}$	10.11	28	66	15.36	1.55	1.76	26.64	877523	$3.04 \times 10^{-5}$
Z-153	$\sim 2 \times 10^{-7}$	10.43	27	60	13.49	1.41	1.58	26.32	761990	$3.45 \times 10^{-5}$
Z-154	$\sim 2 \times 10^{-7}$	10.22	21	60	2.87	0.29	0.31	5.23	85579	$6.12 \times 10^{-5}$
Z-155	$\sim 2 \times 10^{-7}$	10.03	31	77	2.17	0.22	0.25	3.29	23914	$1.38 \times 10^{-4}$

strain localization as a result of initial semi-brittle flow followed by subsequent grain boundary sliding and phase mixing. The strain rate within the shear zone was calculated, using quartz microstructures, to be two orders of magnitude faster than the strain rate occurring in the host rock. Similarly, Holyoke et al. (2014) deformed dolomite aggregates which strain localized as a result of a switch from dislocation creep to diffusion creep due to dynamic recrystallization. Holyoke et al. (2014) used the same methods as I used in this study to determine strain rate within the shear zone and determined that the strain rate in their shear zones were 2-3 orders of magnitude faster than the host rock. They also used dolomite flow laws to estimate strain rate, which were in good agreement.

The strain rate calculations used for the experiments in this study were not performed for the high strain sample because the host rock is deformed, however it is likely that the strain partitioning is similar to the lower strain experiments. The deformation that occurs adjacent to the shear zone in the host rock of the highly strained sample may be the result of changing strain geometry as the sample is increasingly shortened within the assembly, rather than changing rheology of the shear zone, because the microstructures indicate significant grain boundary sliding in the shear zone.

#### 4.3. Shear localization

The formation of shear zones is caused by a process that results in strain weakening, which is commonly associated with grain size reduction. Several studies have demonstrated how strain localizes in response to grain size reduction caused by dislocation creep. Newly recrystallized grains are sufficiently small to activate diffusion related processes which operate at lower stresses than the dislocation creep that is occurring in the larger grains. A switch from dislocation creep to diffusion creep / grain boundary sliding has been proposed to cause strain localization through observations of

experimentally deformed mixtures of anhydrite/calcite (Barnhoorn et al., 2005; Cross and Skemer, 2017), dolomite aggregates (Holyoke et al., 2014), and feldspar aggregates (Tullis et al., 1996). If a switch to diffusion creep and/or grain boundary sliding is activated by a grain size reduction, the initial mechanism causing this reduction is unimportant. Grain size reduction by cataclasis will be indistinguishable from grain size reduction by dislocation creep after small shear strains overprint the microstructures from the brittle deformation. In my samples, it is clear that the material within the pre-existing faults is weaker than the surrounding rock because strain is localized along the cross-cutting faults. The brittle faulting formed fine-grained angular clasts of crushed quartz and feldspar, which were subsequently annealed during the seven-day period between beginning to advance the load column and loading the sample. The grain size in the shear zone is much smaller than the surrounding rock at the time of axial loading. Thus, the deformation mechanism occurring within the shear zone is likely grain size sensitive, resulting in the shear zone being a weaker area than the surrounding rock. Tullis et al., (1990) observed that strain remained localized in a shear zone in pre-faulted feldspar aggregates deformed under conditions where recrystallization-accommodated dislocation creep was the dominant mechanism, similar to my samples. They concluded that this mechanism leads to strain localization when there is a local variation in grain size. However, it is possible that diffusion-accommodated grain boundary sliding is the dominant mechanism acting within feldspar rich zones in the shear zone. However, phases also became mixed in some parts of the shear zone during the initial cataclastic event that formed the pre-fault, enabling grain boundary sliding at low strains. Phases remain mixed at all strains, indicating that grain boundary sliding remains active at higher strains. These results indicate that grain boundary sliding is fundamentally important to the initiation of ductile shear zones, as well as the maintenance of strength contrast for continued localization of strain.

#### 4.4. General implications

In the shear zones of the low to medium strained samples, there is little to no direct evidence of the brittle origin of the fault. The sharp contact between the shear zones and the surrounding rock could be taken as indirect evidence of an original fault, but at higher strains, a strain gradient appears between the surrounding rock and the center of the shear zone, as often is the case for natural shear zones (e.g. Mancktelow and Pennacchioni, 2005). Thus, in natural shear zones, it may be difficult or impossible to determine if the initial localization of strain was related to a brittle pre-cursor. However, brittle deformation can result in a significant reduction in grain size, especially in feldspathic rocks. A switch from brittle deformation to diffusion related processes could represent a potential method for the initiation of strain localization by grain size sensitive creep mechanisms if the right conditions are met. If this situation were to occur in natural rocks containing foliations or other heterogeneities, it would seem likely based upon my results that the other heterogeneities would have little to no effect on the stresses and localization of strain that would occur.

## CHAPTER V

### CONCLUSIONS

I performed a series of experiments on pre-faulted cores the Gneiss Minuti, with the foliation and lineation at a variety of angles to the length of the core. Brittle deformation occurred at low temperature and pressure ( $T = \sim 25^{\circ}\text{C}$ ,  $P_c = \sim 50 - 250 \text{ MPa}$ ) resulting in a through-going fault zone of fine-grained, angular material. When deformed at higher temperature and pressure conditions ( $T = 700^{\circ}\text{C}$ ,  $P_c = 1500 \text{ MPa}$ ), strain localized within the fine-grained fault zones, and little deformation occurred within the surrounding host rock. The following conclusions can be drawn from my results:

1. Grain size reduction at lower temperatures and pressures during the pre-faulting stage created a zone of weakness in which strain continued to localize at final conditions. Up until at least the peak stress, sample strain was accommodated on this ductile shear zone.
2. Within the shear zone, fine grained recrystallized material appears to deform by diffusion accommodated grain boundary sliding. In higher strained samples, the area outside of the shear zone is more transitional; brittle features are apparent in larger feldspar grains while quartz and biotite deform by crystal plastic mechanisms.
3. The orientation of the foliation and lineation of Gneiss Minuti samples did not have any predictable relationship with strength or mode of deformation when a pre-existing fault is present. With much of the strain at final conditions continuing to localize along the ductile shear zone, the strength of the rock will be most affected by these feature, and other heterogeneities are not likely to be important.

4. Evidence of brittle deformation is quickly overprinted by the subsequent microstructures caused by lower stress deformation. Without knowing the complete deformational history of a ductile shear zone, it may not be possible to interpret a brittle pre-cursor.

## REFERENCES

- Barnhoorn, A., Bystricky, M., Kunze, K., Burlini, L., and Burg, J., 2005, Strain localisation in biminerale rocks: Experimental deformation of synthetic calcite–anhydrite aggregates: *Earth and Planetary Science Letters*, v. 240, p. 748–763, doi:10.1016/j.epsl.2005.09.014.
- Boneh, Y., and Skemer, P., 2014, The effect of deformation history on the evolution of olivine CPO: *Earth and Planetary Science Letters*, v. 406, p. 213–222, doi:10.1016/j.epsl.2014.09.018.
- Bürgmann, R., and Dresen, G., 2008, Rheology of the Lower Crust and Upper Mantle: Evidence from Rock Mechanics, Geodesy, and Field Observations: *Annual Review of Earth and Planetary Sciences*, v. 36, p. 531–567, doi:10.1146/annurev.earth.36.031207.124326.
- Cross, A.J., and Skemer, P., 2017, Ultramytonite generation via phase mixing in high-strain experiments: ULTRAMYTONITE GENERATION EXPERIMENTS: *Journal of Geophysical Research: Solid Earth*, doi:10.1002/2016JB013801.
- Dell'Angelo, L.N., and Tullis, J., 1988, Experimental deformation of partially melted granitic aggregates: *Journal of metamorphic Geology*, v. 6, p. 495–515.
- Evans, B., Renner, J., and Hirth, G., 2001, A few remarks on the kinetics of static grain growth in rocks: *International Journal of Earth Sciences*, v. 90, p. 88–103, doi:10.1007/s005310000150.
- Fliervoet, T.F., White, S.H., and Drury, M.R., 1997, Evidence for dominant grain-boundary sliding deformation in greenschist- and amphibolite-grade polymineralic ultramytonites from the Redbank Deformed Zone, Central Australia: *Journal of Structural Geology*, v. 19, p. 1495–1520, doi:10.1016/S0191-8141(97)00076-X.
- Fukuda, J., Holyoke, C.W., and Kronenberg, A.K., 2018, Deformation of Fine-Grained Quartz Aggregates by Mixed Diffusion and Dislocation Creep: *Journal of Geophysical Research: Solid Earth*, v. 123, p. 4676–4696, doi:10.1029/2017JB015133.
- Goodwin, L.B., and Wenk, H.-R., 1995, Development of phyllonite from granodiorite: Mechanisms of grain-size reduction in the Santa Rosa mylonite zone, California: *Journal of Structural Geology*, v. 17, p. 689–707, doi:10.1016/0191-8141(94)00093-F.
- Gottschalk, R.R., Kronenberg, A.K., Russell, J.E., and Handin, J., 1990, Mechanical anisotropy of gneiss: Failure criterion and textural sources of directional behavior: *Journal of Geophysical Research*, v. 95, p. 21613, doi:10.1029/JB095iB13p21613.

- Guermani, A., and Pennacchioni, G., 1998, Brittle precursors of plastic deformation in a granite: an example from the Mont Blanc massif (Helvetic, western Alps): *Journal of Structural Geology*, v. 20, p. 135–148, doi:10.1016/S0191-8141(97)00080-1.
- Handy, M.R., 1986, The structure and rheological evolution of the Pogallo Fault Zone, a deep crustal dislocation in the Southern Alps of Northwestern Italy: PhD thesis, University Basel, Switzerland, 327 p.
- Hansen, L.N., Warren, J.M., Zimmerman, M.E., and Kohlstedt, D.L., 2016, Viscous anisotropy of textured olivine aggregates, Part 1: Measurement of the magnitude and evolution of anisotropy: *Earth and Planetary Science Letters*, v. 445, p. 92–103, doi:10.1016/j.epsl.2016.04.008.
- Hansen, L.N., Zimmerman, M.E., and Kohlstedt, D.L., 2012, Laboratory measurements of the viscous anisotropy of olivine aggregates: *Nature*, v. 492, p. 415–418, doi:10.1038/nature11671.
- Holyoke III, C.W., and Tullis, J., 2006, Formation and maintenance of shear zones: *Geology*, v. 34, p. 105–108, doi:https://doi.org/10.1130/G22116.1.
- Holyoke, C.W., and Kronenberg, A.K., 2010, Accurate differential stress measurement using the molten salt cell and solid salt assemblies in the Griggs apparatus with applications to strength, piezometers and rheology: *Tectonophysics*, v. 494, p. 17–31, doi:10.1016/j.tecto.2010.08.001.
- Holyoke, C.W., Kronenberg, A.K., and Newman, J., 2014, Microstructural evolution during strain localization in dolomite aggregates: *Journal of Structural Geology*, v. 69, p. 449–464, doi:10.1016/j.jsg.2014.04.008.
- Holyoke, C.W., and Tullis, J., 2006, Mechanisms of weak phase interconnection and the effects of phase strength contrast on fabric development: *Journal of Structural Geology*, v. 28, p. 621–640, doi:10.1016/j.jsg.2006.01.008.
- Kilian, R., Heilbronner, R., and Stünitz, H., 2011, Quartz grain size reduction in a granitoid rock and the transition from dislocation to diffusion creep: *Journal of Structural Geology*, v. 33, p. 1265–1284, doi:10.1016/j.jsg.2011.05.004.
- Kronenberg, A.K., Segall, P., and Wolf, G.H., 1990, Hydrolytic weakening and penetrative deformation within a natural shear zone: *Geophysical Monograph*, v. 56, p. 21–36.
- Mancktelow, N.S., and Pennacchioni, G., 2005, The control of precursor brittle fracture and fluid–rock interaction on the development of single and paired ductile shear zones: *Journal of Structural Geology*, v. 27, p. 645–661, doi:10.1016/j.jsg.2004.12.001.
- Mitra, G., 1984, Brittle to ductile transition due to large strains along the White Rock thrust, Wind River mountains, Wyoming: *Journal of Structural Geology*, v. 6, p. 51–61, doi:10.1016/0191-8141(84)90083-X.
- Paterson, M.S., and Olgaard, D.L., 2000, Rock deformation tests to large shear strains in torsion: *Journal of Structural Geology*, v. 22, p. 1341–1358, doi:10.1016/S0191-8141(00)00042-0.

- Segall, P., and Simpson, C., 1986, Nucleation of ductile shear zones on dilatant fractures: , p. 4.
- Shea, W.T., and Kronenberg, A.K., 1993, Strength and anisotropy of foliated rocks with varied mica contents: *Journal of Structural Geology*, v. 15, p. 1097–1121, doi:10.1016/0191-8141(93)90158-7.
- Sibson, R.H., 1977, Fault rocks and fault mechanisms: *Journal of the Geological Society*, v. 133, p. 191–213, doi:10.1144/gsjgs.133.3.0191.
- Stünitz, H., and Gerald, J.F., 1993, Deformation of granitoids at low metamorphic grade. II: Granular flow in albite-rich mylonites: *Tectonophysics*, v. 221, p. 299–324.
- Tullis, J., Dell'Angelo, L., and Yund, R.A., 1990, Ductile shear zones from brittle precursors in feldspathic rocks: The role of dynamic recrystallization, in Duba, A.G., Durham, W.B., Handin, J.W., and Wang, H.F. eds., *Geophysical Monograph Series*, Washington, D. C., American Geophysical Union, v. 56, p. 67–81, doi:10.1029/GM056p0067.
- Tullis, J., and Yund, R.A., 1991, Diffusion creep in feldspar aggregates: experimental evidence: *Journal of Structural Geology*, v. 13, p. 987–1000, doi:10.1016/0191-8141(91)90051-J.
- Tullis, J., and Yund, R.A., 1987, Transition from cataclastic flow to dislocation creep of feldspar: Mechanisms and microstructures: *Geology*, v. 15, p. 606–609, doi:10.1130/0091-7613(1987)15<606:TFCFTD>2.0.CO;2.
- Tullis, J., Yund, R., and Farver, J., 1996, Deformation-enhanced fluid distribution in feldspar aggregates and implications for ductile shear zones: *Geology*, v. 24, p. 63–66, doi:https://doi.org/10.1130/0091-7613(1996)024<0063:DEFDIF>2.3.CO;2.
- Zurbriggen, R., Kamber, B.S., Handy, M.R., and Nægler, T.F., 1998, Dating synmagmatic folds: a case study of Schlingen structures in the Strona-Ceneri Zone (Southern Alps, northern Italy): *DATING SYN-MAGMATIC FOLDS*: *Journal of Metamorphic Geology*, v. 16, p. 403–414, doi:10.1111/j.1525-1314.1998.00145.x.

## APPENDICES

## APPENDIX A

### EXPERIMENTS

The following appendix contains a list of the experiments and their conditions performed during this study, including those not used in the main text.

Table A1. List of all experiments performed during this study

Experiment	Material	Orientation	Temperature (°C)	Strain Rate (s <sup>-1</sup> )	Pre-hit strain(%)	Applied Strain (%)	Peak Stress (MPa)	Used in study	Comments
Z-128	GM 17 4b	F90-L90	750	1.6X10 <sup>-7</sup>	16.2	34.4	850	No	Localized strain along pre-fault
Z-130	GM 17 4b	F90-L90	750	-	-	-	-	No	Hydrostatic experiment, quenched immediately after reaching conditions. Original sample length not in records
Z-131	GM 17 4b	F90-L90	800	1.6X10 <sup>-6</sup>	11.9	30.7	600	No	Reaction, possible melt
Z-134	GM 17 4b	F90-L90	750	6.8X10 <sup>-7</sup>	11.8	31.0	670	No	Reaction, possible melt
Z-135	GM 17 4b	F90-L90	750	-	-	-	-	No	Hydrostatic experiment left at conditions 1 hr
Z-140	GM 01 AB	F90-L90	750	6.8X10 <sup>-7</sup>	6.2	24.9	680	No	Reaction, possible melt
Z-142	GM 01 AB	F90-L90	750	6.8X10 <sup>-7</sup>	3.2	12.6	450	No	First experiment used with tiny pistons. Issue with TC
Z-143	GM 01 AB	F90-L90	700	1.6X10 <sup>-7</sup>	3.4	9.7	720	No	Issues with maintaining pressure, sudden pressure drops
Z-148	GM 01 AB	F45-L45	700	1.6X10 <sup>-7</sup>	8.9	15.4	1110	Yes	Localized strain along pre-fault
Z-150	GM 01 AB	F0-L45	700	1.6X10 <sup>-7</sup>	7.5	14.0	1040	Yes	Localized strain along pre-fault
Z-151	GM 01 AB	F90-L90	700	1.6X10 <sup>-7</sup>	7.0	15.5	930	Yes	Localized strain along pre-fault
Z-152	GM 01 AB	F0-L0	700	1.6X10 <sup>-7</sup>	7.6	15.4	1210	Yes	Localized strain along pre-fault
Z-153	GM 01 AB	F0-L90	700	1.6X10 <sup>-7</sup>	8.1	13.5	1010	Yes	Localized strain along pre-fault
Z-154	GM 01 AB	F0-L0	700	1.6X10 <sup>-7</sup>	7.1	2.9	560	Yes	Localized strain along pre-fault
Z-155	GM 01 AB	F45-L45	700	1.6X10 <sup>-7</sup>	7.6	2.2	480	Yes	Localized strain along pre-fault
Z-156	GM 01 AB	F45-L45	700	-	-	-	-	Yes	Hydrostatic experiment left at conditions 1 hr
Z-157	GM 01 AB	F45-L45	700	-	-	-	-	Yes	Hydrostatic experiment, left at conditions 7 days
Z-159	GM 01 AB	F45-L45	700	1.6X10 <sup>-7</sup>	10.5	44.0	1110	Yes	Pressurized to 250 MPa
Z-163	Enfield Aplite	-	25	-	1.7	-	-	Yes	Pressurized to 300 MPa. Sample fell apart, could not measure length after pressurization
Z-164	Sioux Quartzite	-	25	-	-	-	-	No	Pressurized to 250 MPa. Sample fell apart, could not measure length after pressurization
Z-165	Black Hills Quartzite	-	25	-	-	-	-	No	Pressurized to 250 MPa. Sample fell apart, could not measure length after pressurization
Z-166	GM 01 AB	F0-L0	800	-	0.4	-	-	No	Very low pre-hit strain, but a fault was formed
Z-168	Tanna Quartzite	-	25	-	0.0	-	-	No	Pressurized to 250 MPa. No observable pre-hit strain
Z-169	Tanna Quartzite	-	800	1.6X10 <sup>-6</sup>	0.0	37.2	950	No	No observable pre-hit strain

## APPENDIX B

### SELECTED EXPERIMENTS NOT USED IN THE MAIN STUDY

The following appendix contains selected figures from experiments that were not discussed in the main study.

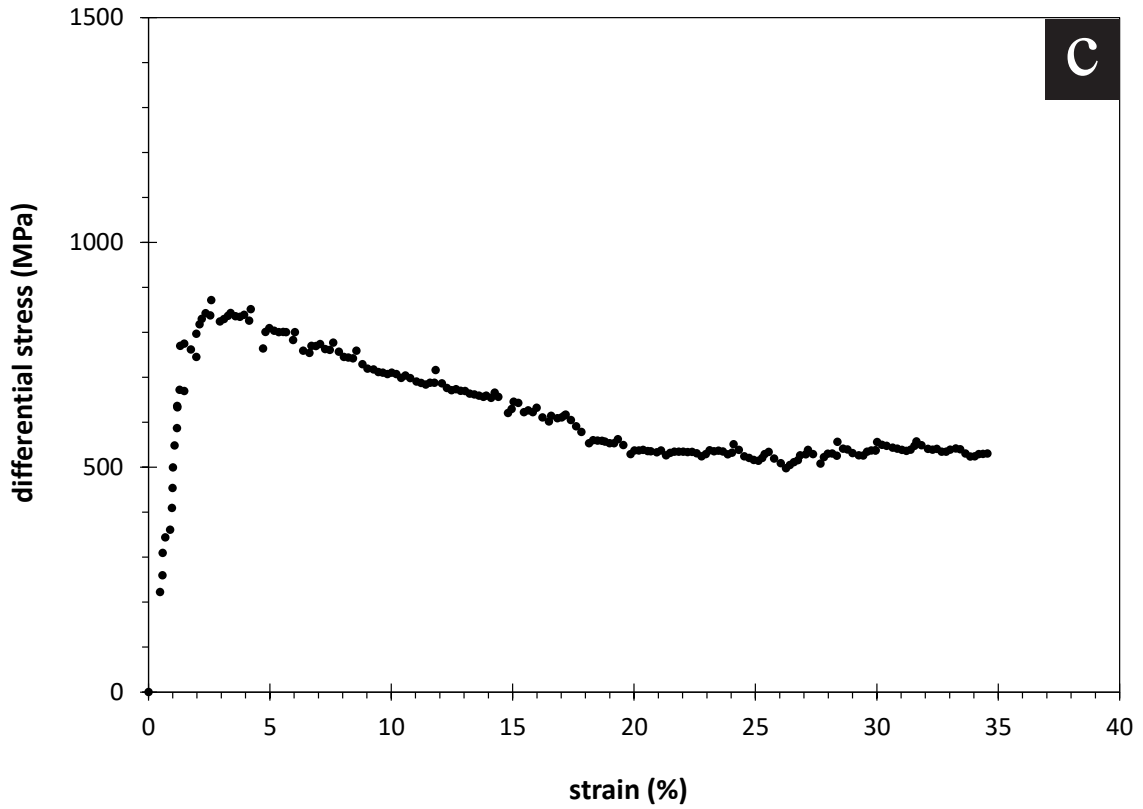
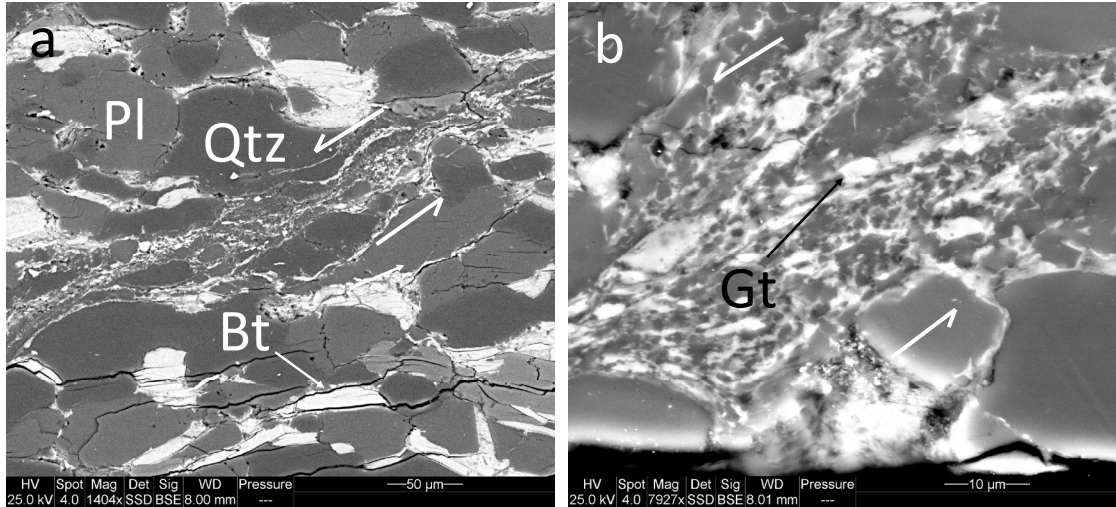


Figure B1. Sample Z-128:  $T = 750^{\circ}\text{C}$ ,  $P_c = 1500 \text{ MPa}$ ,  $\dot{\epsilon} = 1.6 \times 10^{-7} \text{ s}^{-1}$ . A) A shear zone is present which cross-cuts this sample. B) The shear zone contains some reaction products, including garnet. C) Mechanical data from experiment.

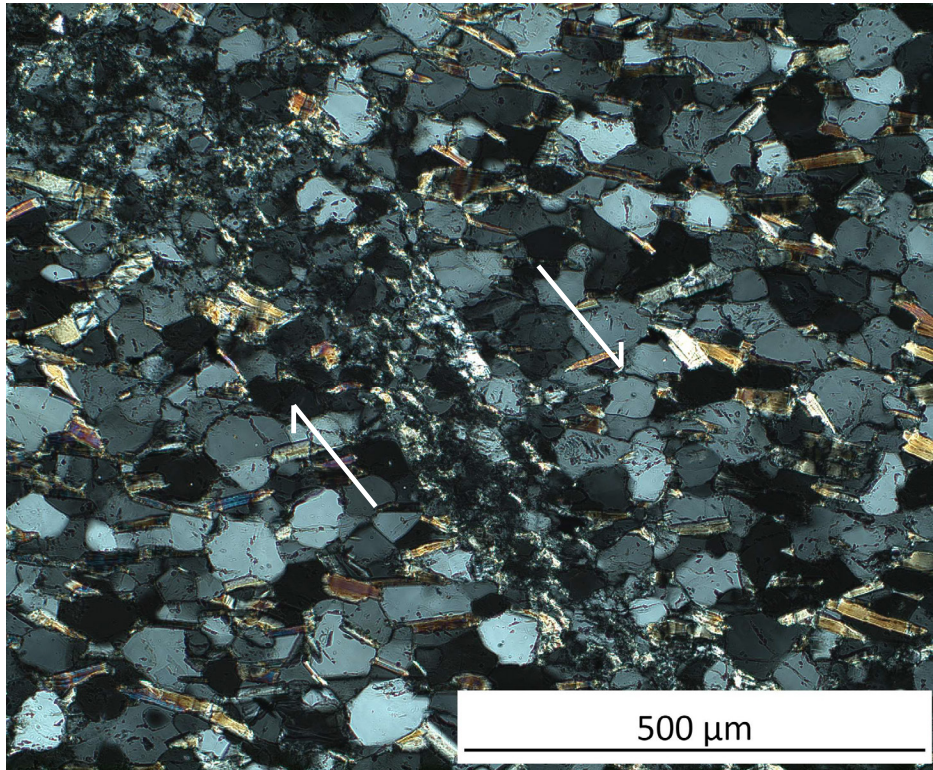


Figure B2. Sample Z-130:  $T = 750^{\circ}\text{C}$ ,  $P_c = 1500 \text{ MPa}$ , hydrostatic. The ductile shear zone that cross cuts this sample was likely caused by pre-hit deformation.

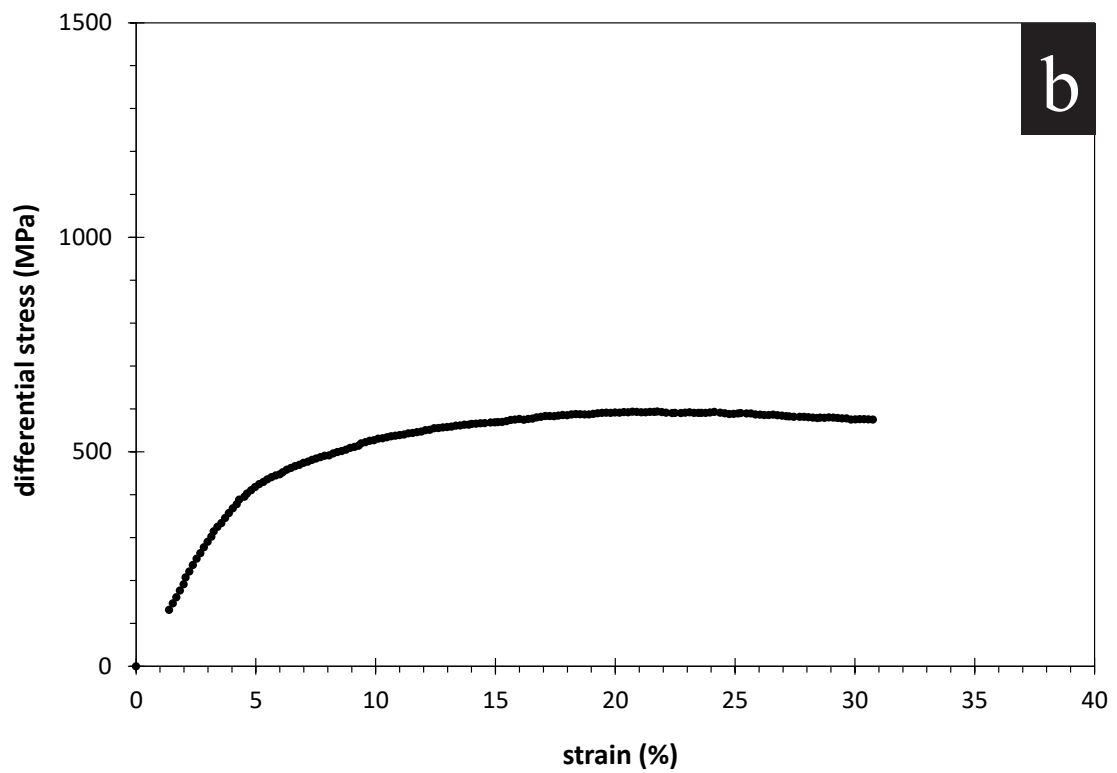
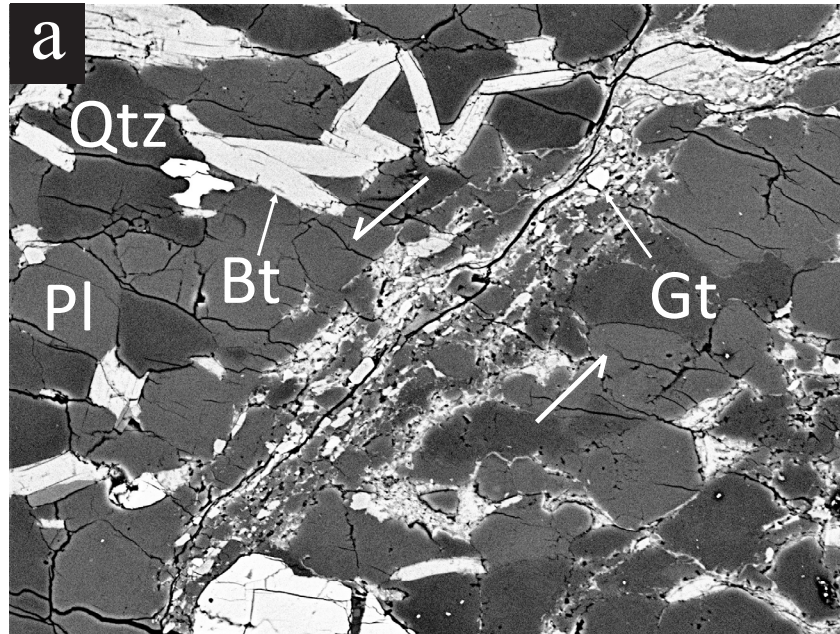


Figure B3. Sample Z-131:  $T = 800^{\circ}\text{C}$ ,  $P_c = 1500 \text{ MPa}$ ,  $\dot{\epsilon} = 1.6 \times 10^{-6} \text{ s}^{-1}$ . A) A shear zone, which contains metamorphic reactions, cross-cuts this sample. B) Mechanical data from experiment.

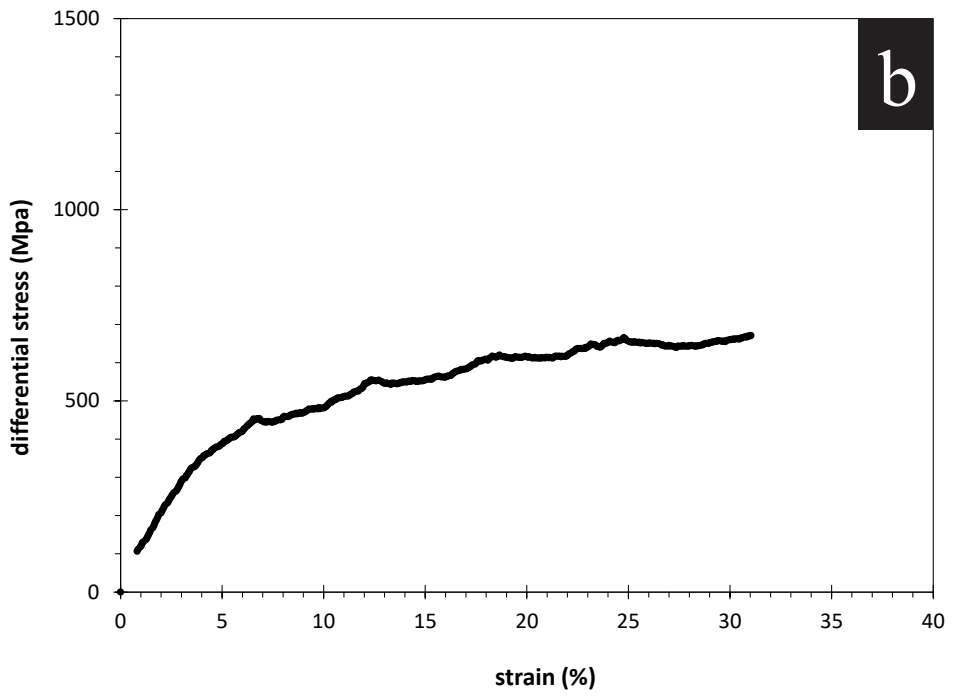
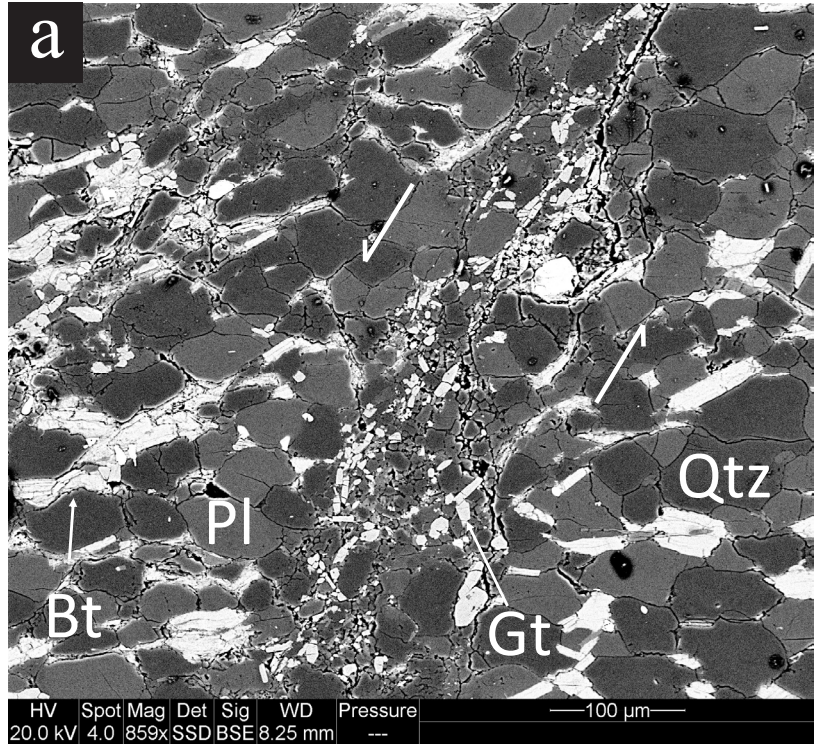


Figure B4. Sample Z-134:  $T = 750^{\circ}\text{C}$ ,  $P_c = 1500 \text{ MPa}$ ,  $\dot{\epsilon} = 6.8 \times 10^{-7} \text{ s}^{-1}$ . A) A shear zone, which contains metamorphic reactions, cross-cuts this sample. B) Mechanical data from experiment.

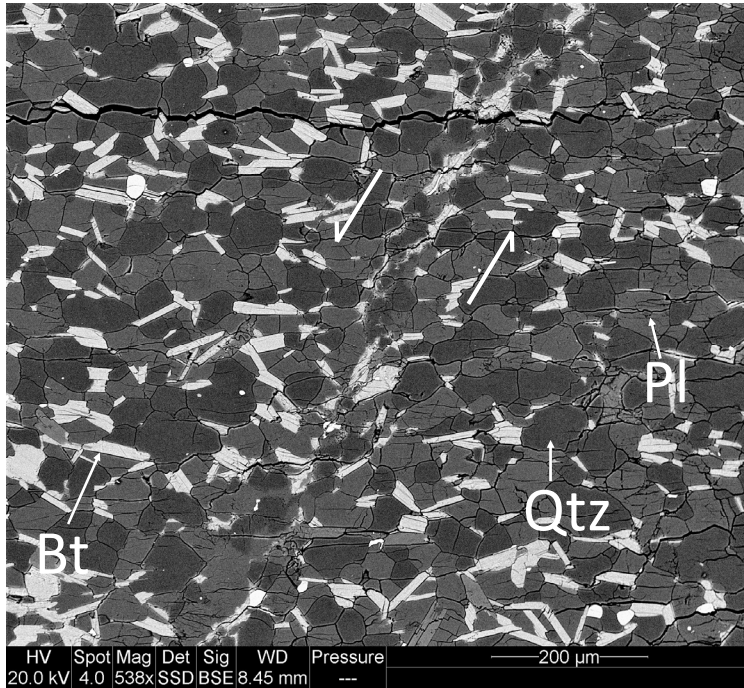


Figure B5. Sample Z-135:  $T = 750^{\circ}\text{C}$ ,  $P_c = 1500 \text{ MPa}$ , hydrostatic. The ductile shear zone that cross-cuts this sample is likely due to pre-hit deformation.

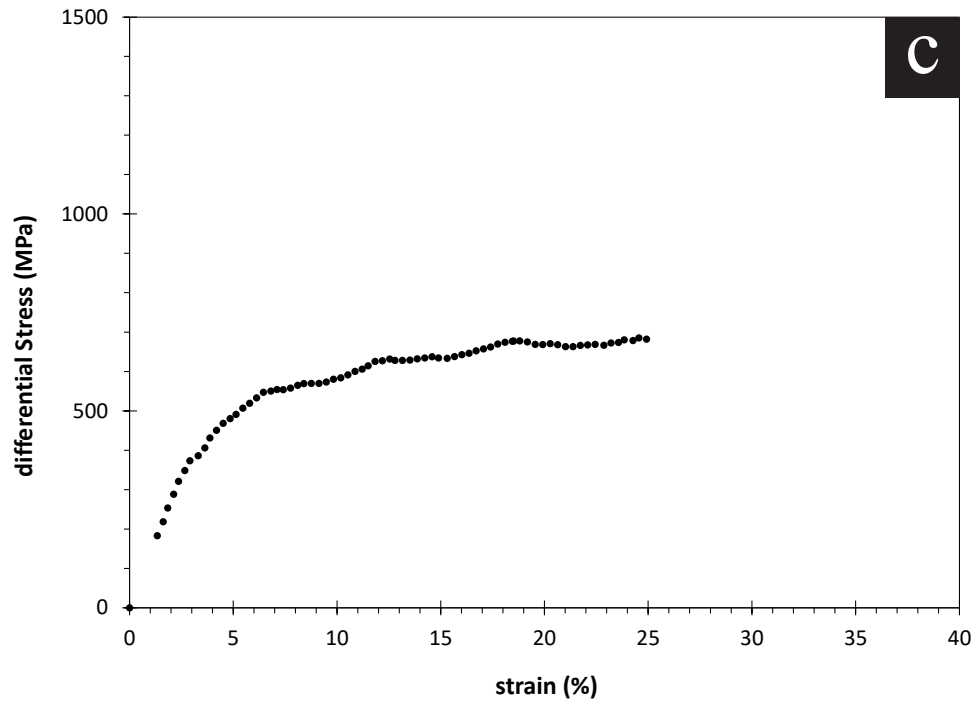
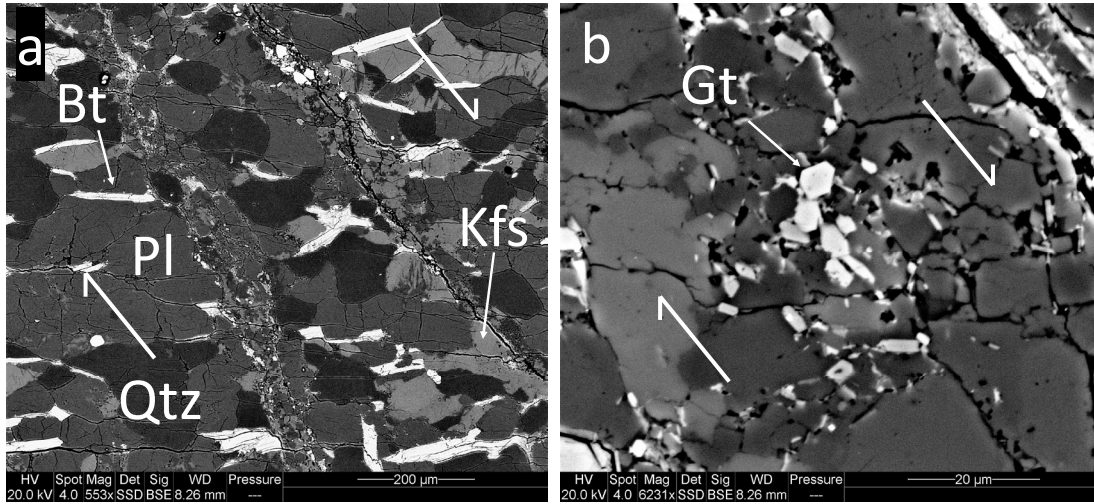


Figure B6. Sample Z-140:  $T = 750^{\circ}\text{C}$ ,  $P_c = 1500 \text{ MPa}$ ,  $\dot{\epsilon} = 6.8 \times 10^{-7} \text{ s}^{-1}$ . A) A ductile shear zone cross-cuts the sample. B) The shear zone contains metamorphic reaction products such as garnet and melt. C) Mechanical data from experiment.

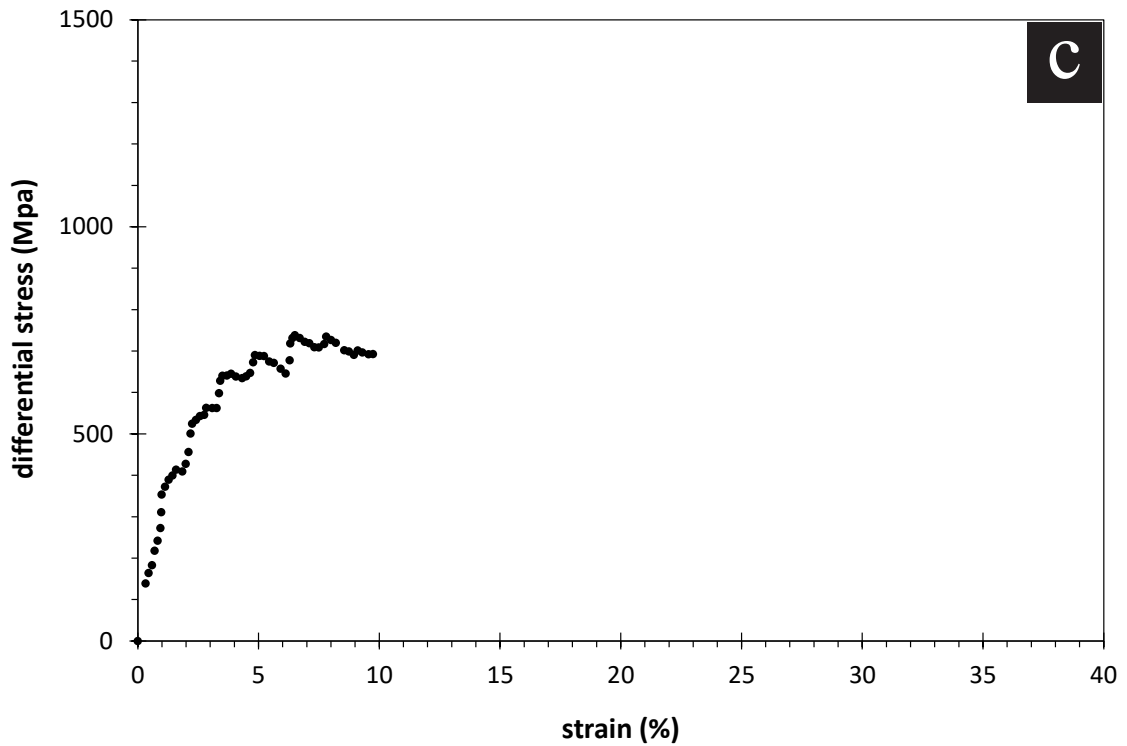
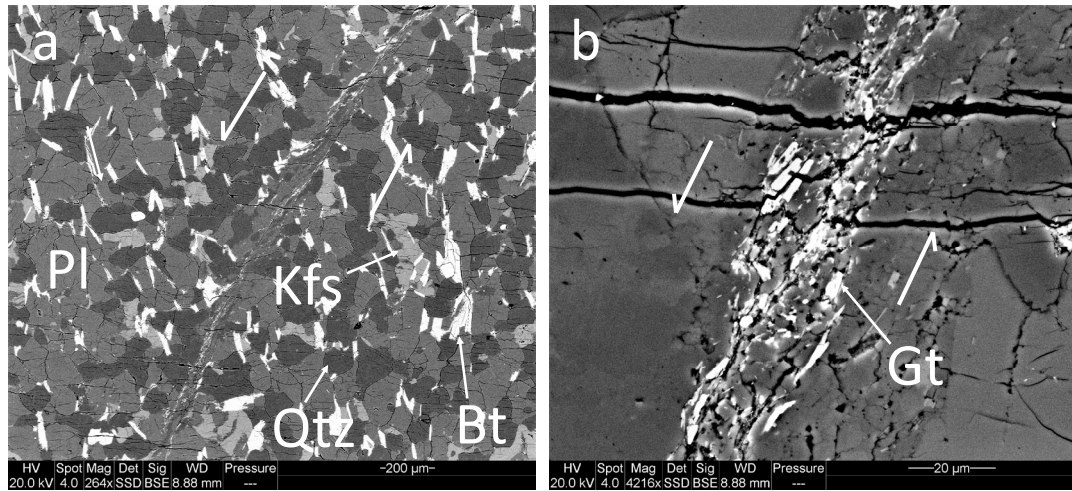


Figure B7. Sample Z-143:  $T = 700^{\circ}\text{C}$ ,  $P_c = 1500 \text{ MPa}$ ,  $\dot{\epsilon} = 1.6 \times 10^{-7} \text{ s}^{-1}$ . This sample was not used because of significant pressure fluctuations during deformation. A) A shear zone cross-cuts this sample. B) The shear zone appears to contain some metamorphic reaction products. C) Mechanical data from experiment.

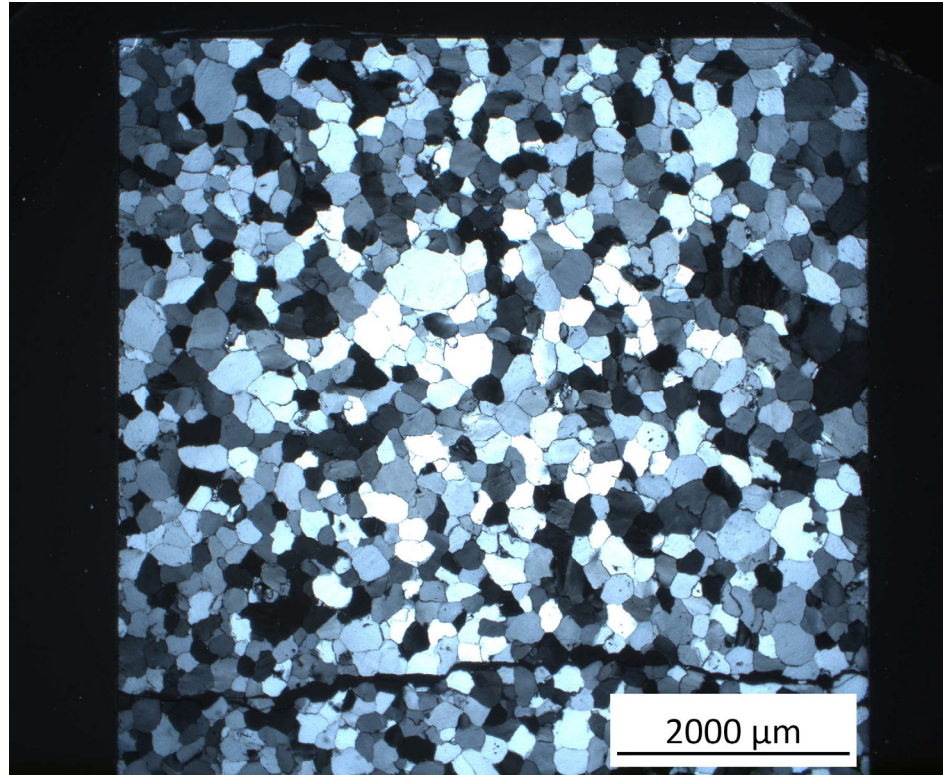


Figure B8. Sample Z-168:  $T = 25^{\circ}\text{C}$ ,  $P_c = 250 \text{ MPa}$ , hydrostatic. Low pressure hydrostatic experiment with a new base plate. No evidence of brittle faulting is present. There is no displacement along the horizontal crack, which likely formed during unloading. The base plate used in previous experiments had been subjected to overheating events causing deformation, which likely resulted in samples being positioned slightly off axis within the assembly, resulting in stress concentrations and brittle deformation during pressurization.

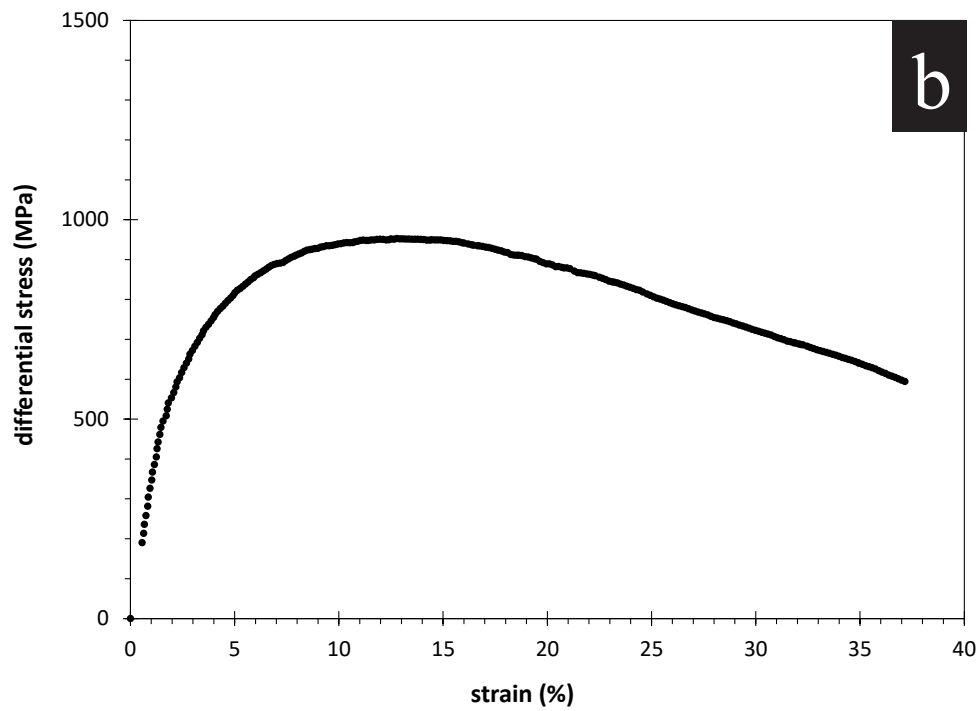
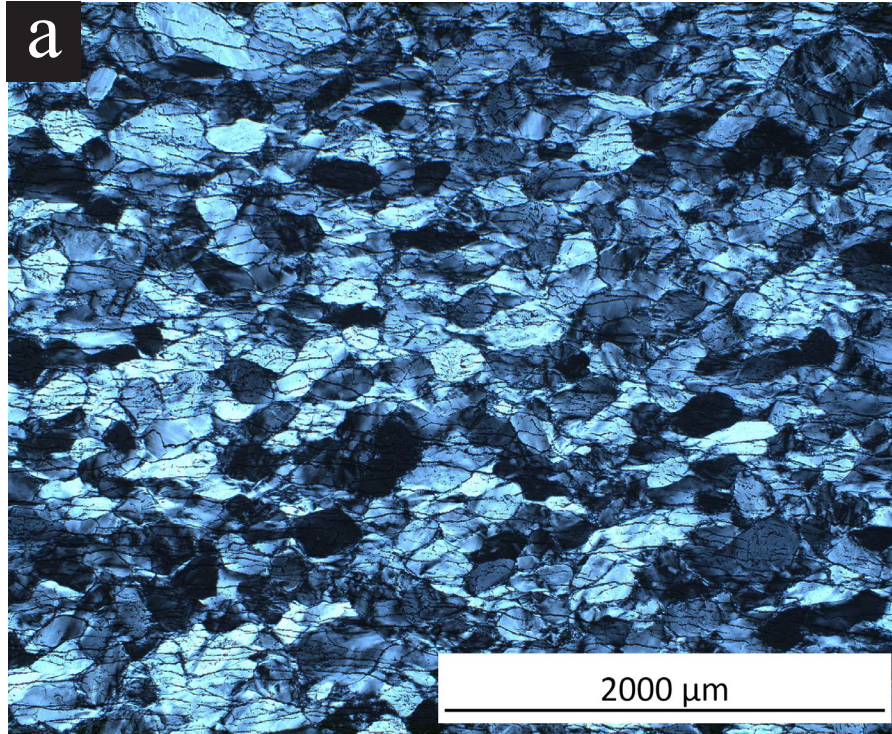


Figure B9. Sample Z-169, Tanna Quartzite:  $T = 800^{\circ}\text{C}$ ,  $P_c = 1500 \text{ MPa}$ ,  $\dot{\epsilon} = 1.6 \times 10^{-6} \text{ s}^{-1}$ . A) Deformation occurred by dislocation creep and the sample contained no evidence of pre-hit deformation. B) Mechanical data from experiment.

## APPENDIX C

### MAGNETIC ANISOTROPY OF GNEISS MINUTI

The following is a study performed on the Gneiss Minuti, testing its magnetic properties and how they vary with the foliation. This was a required term paper for the Environmental Magnetism course that I attended in the fall of 2019.

## Abstract

In this study the magnetic properties of a fine-grained gneiss (Gneiss Minuti) are investigated with the intent of discovering if there is magnetic anisotropy related to the foliation plane. Cylinders cored at varying angles ( $0^\circ$ ,  $45^\circ$ , and  $90^\circ$ ) to the foliation are subjected to magnetic hysteresis analysis in various orientations. Isothermal remanence (IRM) acquisition is also performed and coercivity of remanence ( $H_{cr}$ ) measured. Samples of mica (biotite and phlogopite) are also measured to evaluate the potential effect of mica orientation on magnetic anisotropy. The three Gneiss Minuti cylinders are found to have highly variable levels of magnetic concentration, with ferrimagnetic contribution ranging from 6 to 26% of the sample's magnetization. Optical and SEM images show that dispersion of oxide grains is wide enough to cause significant variations of their presence within a cylinder depending on the location at which it is cored. However, magnetic mineralogy parameters indicate that all cylinders contain a ferrimagnetic phase, likely magnetite. The magnetic concentration parameters and coercivity of remanence display a magnetic anisotropy with an easy orientation of magnetization parallel to the foliation, and a hard orientation perpendicular to the foliation. The easy magnetization direction is defined by higher magnetic concentration values and lower coercivity. The observed magnetic anisotropy may be in part a result of a lattice preferred orientation of ferrimagnetic grains. The anisotropy is also likely due a shape preferred orientation, which is supported by thin section and SEM imaging showing that oxide grains tend to be elongate in the direction of the foliation.

## 1. Introduction

Highly strained metamorphic rocks develop a foliated texture which is defined by the alignment of mineral grains as well as their preferred crystallographic orientation. Foliation can produce anisotropy for various rock properties. Gottschalk et al. (1990) demonstrated that cylinders of gneiss compressed at varying angles to its foliation have significant strength anisotropy. It is also possible that foliation can influence the magnetic properties of a metamorphic rock. Iron bearing minerals, and to a lesser extent remanence bearing iron oxides, are present in most igneous and metamorphic rocks. Metamorphism may cause a shape or crystallographic orientation of remanence bearing minerals that leads to magnetic anisotropy in relation to foliation. Measuring the anisotropy of rock magnetism has been shown to be useful in the characterization of fabric and extent of strain in metamorphic rocks (Mamtani et al., 2011).

In this study, a fine-grained gneiss (Gneiss Minuti) with a well-defined foliation plane is analyzed for magnetic properties. The potential relationship between magnetic anisotropy and foliation is experimentally investigated by measuring the magnetic properties of the gneiss minuti at varying angles to the foliation plane. Some individual mica samples (biotite and phlogopite) of unknown origins were also evaluated for magnetic properties in relation to crystallographic orientation since the foliation of the gneiss minuti is largely defined by the orientation of mica grains. With the data obtained in this experiment, the extent of magnetic anisotropy of the gneiss minuti may be evaluated, as well as the potential mechanism which causes it.

## 2. Materials and Methods

### 2.1. Gneiss Minuti

The gneiss minuti is a fine-grained gneiss derived from the Strona-Ceneri Zone of northern Italy, located in the western part of the southern Alps (Fig. C1). The gneiss in this area was emplaced in the late Ordovician and subsequent deformation is related to

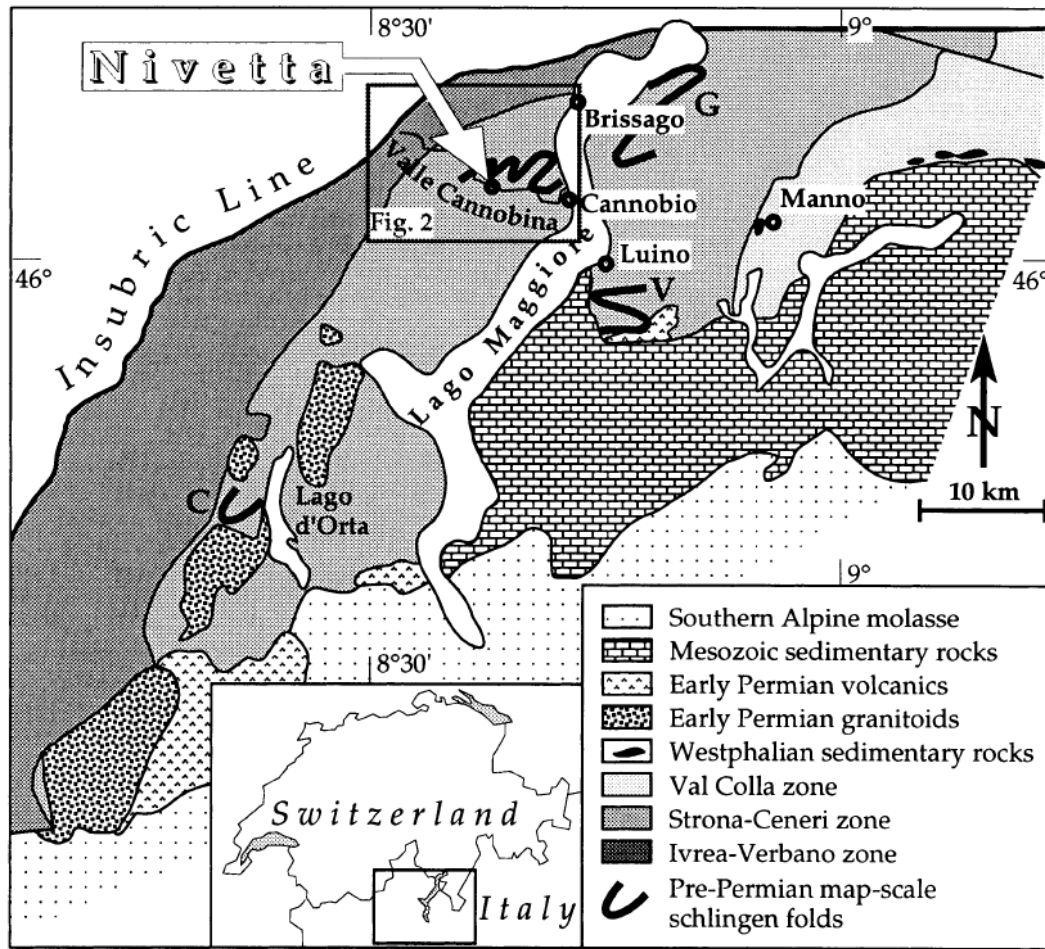


Figure C1. Geologic map of gneiss minuti locality, taken from Zurbriggen et al, (1998).

the Variscan orogeny. Zurbriggen et al. (1998) estimated the temperature and pressure of formation to be about 500° C and 500MPa. The Gneiss Minuti layer used in this study is predominately composed of quartz, plagioclase feldspar, and biotite, the quantities of which are estimated to be ~40, 45, and 15% respectively. Accessory minerals include muscovite, garnet, orthoclase, and oxides (Fig. C2).

1.5mm diameter cylinders were cored with the foliation perpendicular (Pr cylinder), parallel (Pa cylinder), and 45° (45° cylinder) to the cylinder length. Cylinder masses are 13.192mg, 11.858mg, and 5.992mg respectively. The cylinders were tested for hysteresis parameters using the Alternating Gradient Magnetometer (AGM). Each cylinder was tested at varying orientations of the cylinder length to the direction of the applied field (0°, 90°, 180° 270°). Each orientation corresponds to an angle between the foliation and the applied field, which varies depending on the orientation of the foliation within the cylinder (fig. C3). Four additional orientations were measured for the Pa cylinder, including a 45 and 135° orientation, and two “rolls” in the 0° orientation where the cylinder was rolled 45° and 90°.

Hysteresis parameters were measured for each orientation by subjecting the sample to a range of positive and negative field (-500 – 500 mT) and measuring the induced magnetization. Measured hysteresis parameters are: Coercivity (Hc), saturation remanence (Mrs), magnetic saturation (Ms), initial slope (Is), and slope correction (SC). Initial slope (Is) may be interpreted similarly to low field susceptibility, as they are both a measure of a materials magnetization response to low field values (App. CA). Isothermal remanence magnetization (IRM) acquisition and coercivity of remanence (Hcr) tests were also conducted, and a first order reversal curve (FORC) was applied to the Pr cylinder with the foliation orientated 0° to the field. Hcr' was calculated by using linear interpolation to find the field value by which 50% IRM is acquired. This value is used for the parameter Hcr'/Hcr, which can indicate the presence of titanium in magnetite (App.

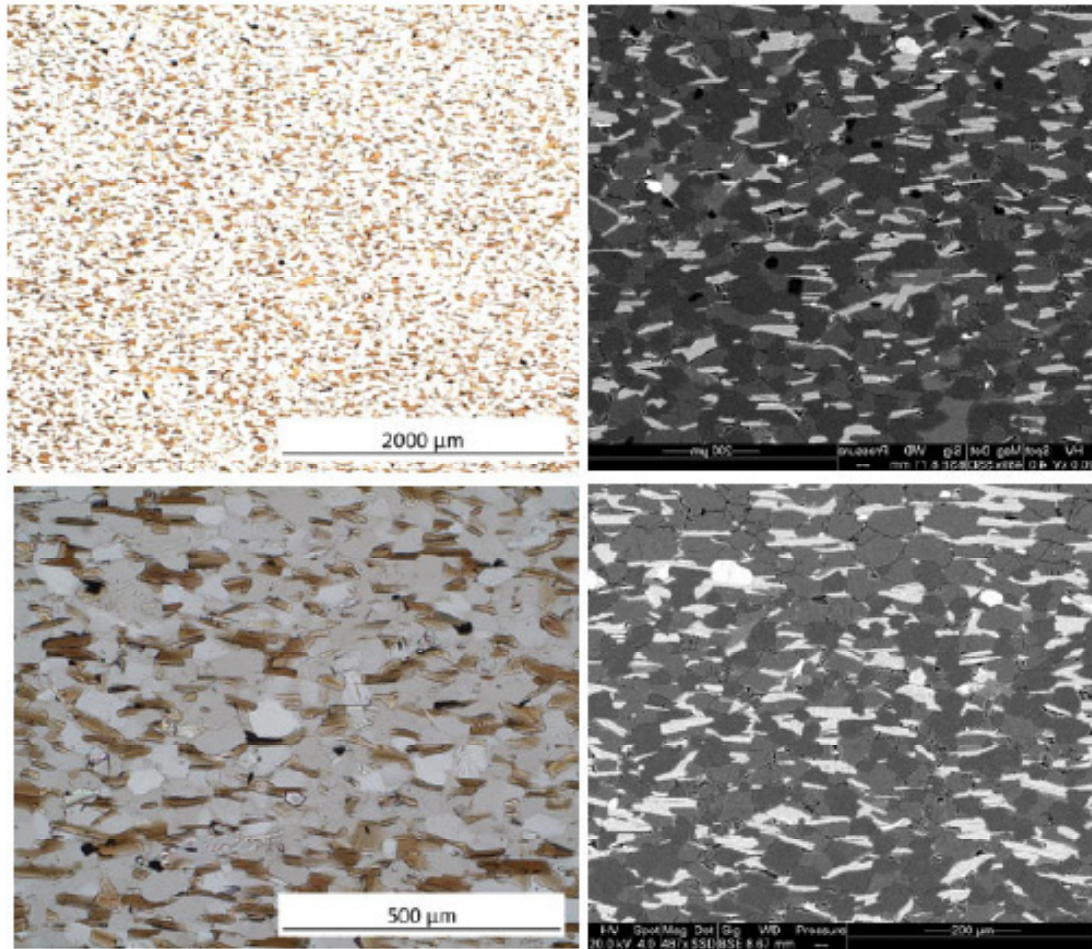


Figure C2. Plane light petrographic (right) and SEM (left) images of the Gneiss Minuti layer used in this study.

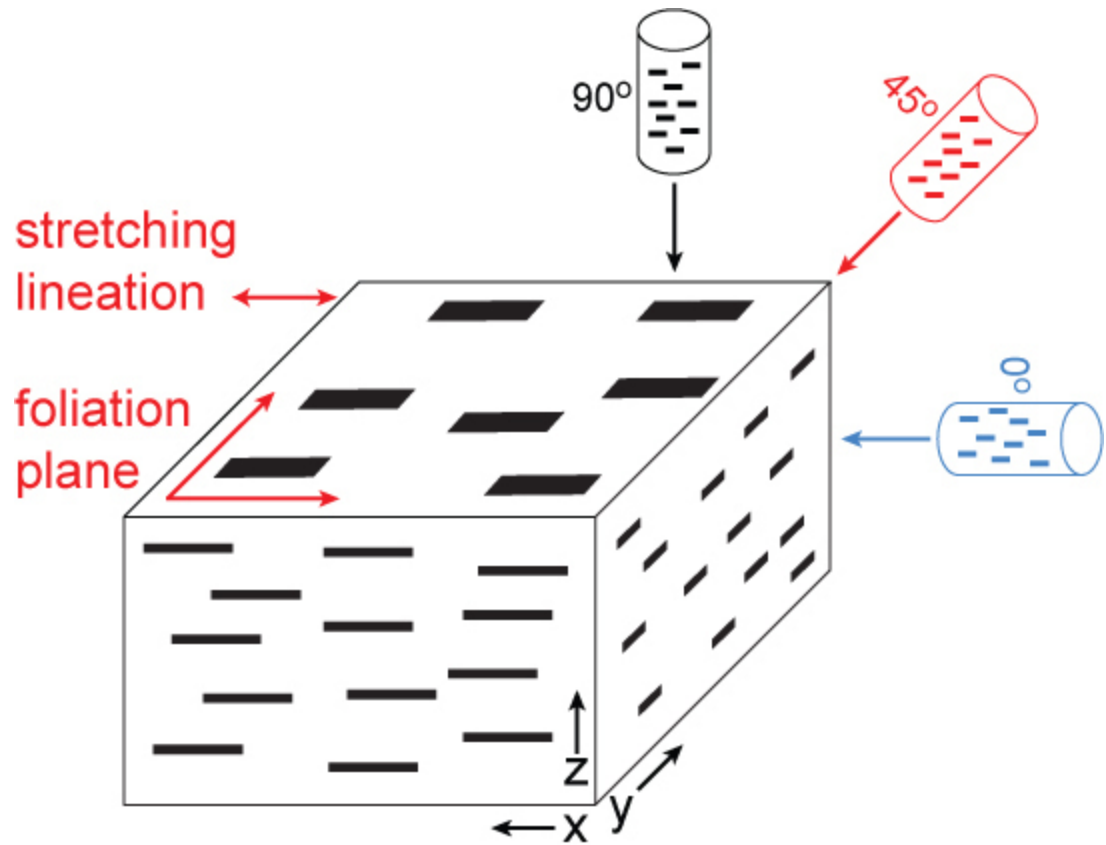


Figure C3. Cylinder orientations used in this study.

A). The percent of initial slope attributed to ferrimagnetic contribution was obtained by subtracting high field slope (400-500mT) from low field slope (0-300mT), dividing low field slope by this value and multiplying by 100.

## 2.2. Biotite and Phlogopite

One biotite sample of unknown origin was tested in several different orientations with respect to crystallographic axes. The basal plane was placed in a horizontal position at  $0^\circ$  to the applied field, and then rotated to be at  $90^\circ$  to the applied field. These orientations simulate the position of the biotite within the Gneiss Minuti samples when the foliation is orientated at  $0/180^\circ$  (parallel) and  $90/270^\circ$  (perpendicular) respectively. Another suite of biotite orientations were measured by placing the basal plane at  $0^\circ$  to the applied field, but in a vertical position. The sample was then rotated  $45^\circ$  and  $90^\circ$ . This was done to test potential magnetic variations along the A and B axes. One phlogopite sample in one orientation (basal plane horizontal at  $0^\circ$ ) was also measured.

## 3. Results

Magnetic hysteresis was observed for all cylinders, with the most pronounced being in the Pr cylinder with foliation orientated at  $0^\circ$  to the applied field (Fig. C4).

### 3.1. Magnetic concentration parameters for Gneiss Minuti cylinders

The Pr cylinder has the largest values for all magnetic concentration parameters ( $M_s$ ,  $M_r$ , and  $I_s$ ) suggesting that it has a higher ferrimagnetic concentration than the other two cylinders (App. A, Table 1, Figs. C5, C6, and C7). Both the Pr and Pa cylinder exhibit a variation in their concentration parameters with orientation of foliation to the field. For all concentration parameters, the Pr and Pa cylinders have higher values when the foliation plane is orientated parallel with the applied field ( $0^\circ$ ,  $180^\circ$ ) compared to the when the foliation plane is perpendicular to the field ( $90^\circ$ ,  $270^\circ$ ). The orientations used for the  $45^\circ$  cylinder all resulted in the foliation being close to  $45^\circ$  to the field (Fig. C3). It

Table 1. Magnetic hysteresis parameters for gneiss minuti cylinders and mica samples.

sample / orientation	H/F (°)	Hc (mT)	Mr ( $\mu\text{Am}^2 \text{kg}^{-1}$ )	Ms ( $\text{mAm}^2 \text{kg}^{-1}$ )	Is ( $\text{mAm}^2 \text{T}^{-1} \text{kg}^{-1}$ )	S.C. ( $\text{mAm}^2 \text{T}^{-1} \text{kg}^{-1}$ )	Hcr (mT)	Hcr/Hc	Mrs/Ms	Mrs/Is $\text{mT}^{-1}$
Pr 0	0	4.63	308.1	8.14	46.57	-59.07	23.03	4.97	0.038	6.62
Pr 90	90	5.78	264.4	5.70	36.37	-55.82	28.37	4.90	0.046	7.27
Pr 180	180	4.50	323.7	7.36	59.3	-59.85	21.34	4.74	0.044	5.46
Pr 270	270	6.27	247.5	5.23	33.12	-55.77	30.32	4.83	0.047	7.47
Pa 90	0	7.31	161.2	1.43	14.3	-60.11	20.15	2.76	0.113	11.27
Pa 180	90	7.91	162.4	1.30	12.38	-51.06	24.15	3.06	0.125	13.12
Pa 270	180	7.64	171.7	1.43	14.12	-58.88	20.33	2.66	0.120	12.16
Pa 0	270	9.08	114.7	1.00	8.842	-55.63	27.92	3.07	0.115	12.97
Pa OR45	0	8.24	151.2	1.22	11.1	-51.89	25.12	3.05	0.124	13.62
Pa OR90	0	8.50	167.6	1.25	12.36	-48.43	23.70	2.79	0.134	13.56
Pa 135	135	7.84	172	1.37	13.07	-54.77	20.33	2.59	0.125	13.16
Pa 45	45	8.14	150	1.37	12.79	-51.98	20.66	2.54	0.109	11.73
45° 0	45	8.24	127.7	0.99	8.934	-52.69	30.43	3.70	0.129	14.29
45° 90	45	8.50	123	1.00	9.24	-47.41	30.49	3.59	0.123	13.31
45° 180	45	8.14	124.9	1.04	9.468	-51.54	28.21	3.47	0.120	13.19
45° 270	45	7.85	134	1.08	9.744	-54.77	29.63	3.77	0.125	13.75
Bi C 0	0	11.70	71.22	0.71	6.327	-176.1	47.51	4.06	0.100	11.26
Bi C 90	90	8.69	72.93	0.71	5.685	-132.5	66.52	7.65	0.103	12.83
Bi AB 0	0	12.22	65.86	0.73	5.898	-173.8	56.16	4.60	0.090	11.17
Bi AB 45	45	8.43	95.93	0.76	5.973	-168.5	58.50	6.94	0.127	16.06
Bi AB 90	90	9.60	76.22	0.73	6.095	-170.6	63.75	6.64	0.105	12.51
Ph C 0	0	20.17	173	0.48	3.592	6.556	62.05	3.08	0.360	48.16

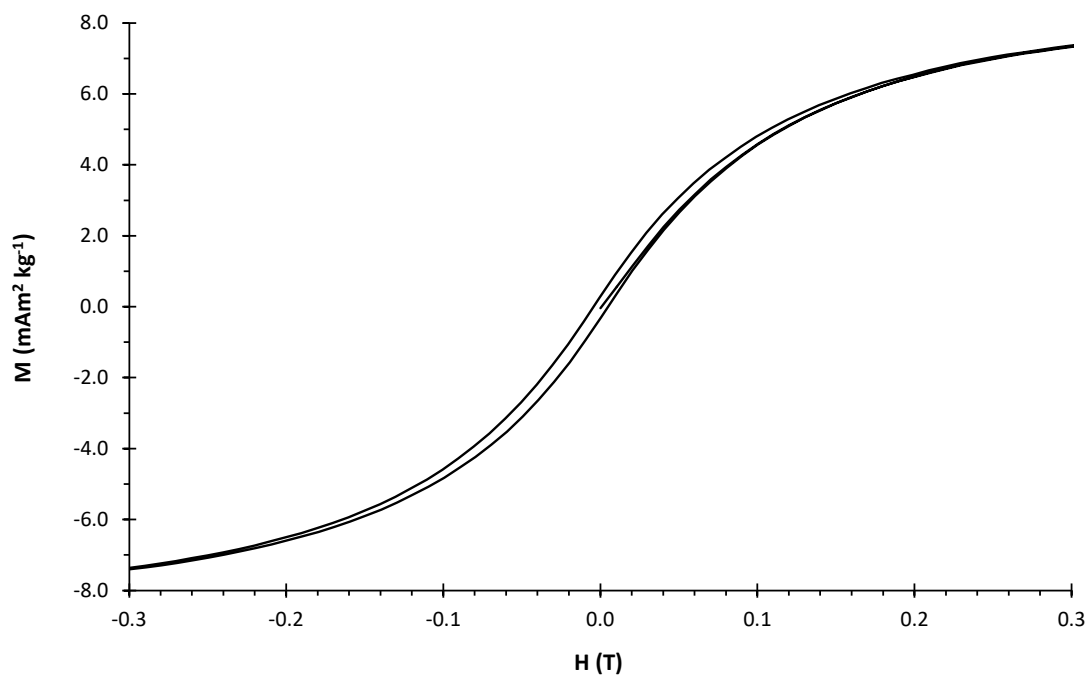
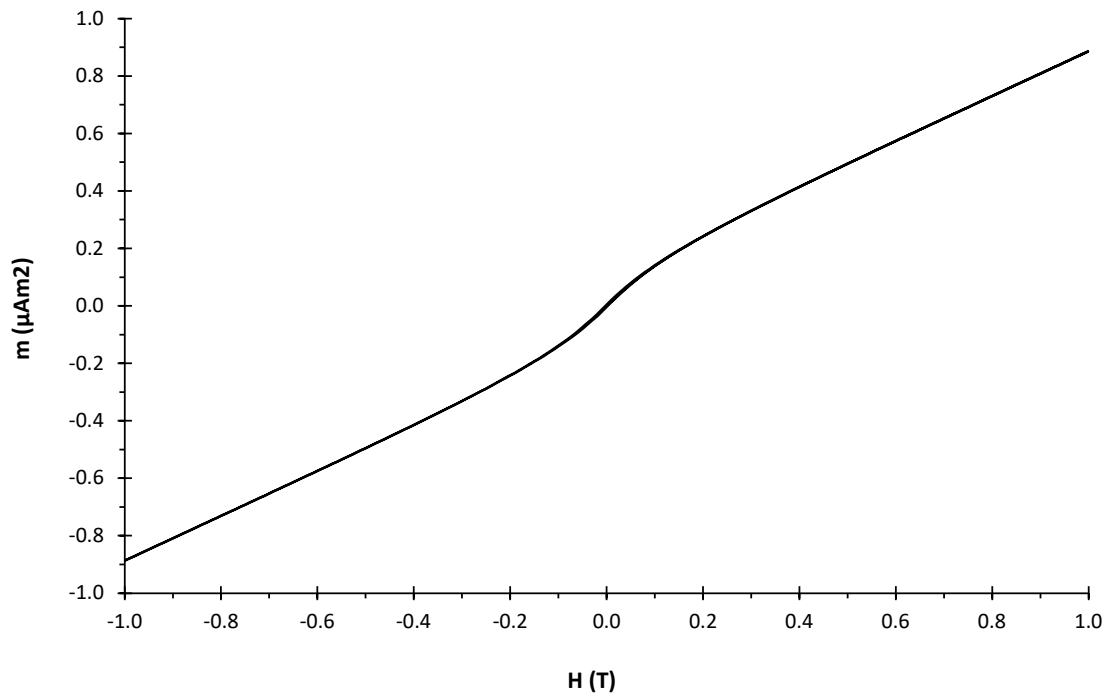


Figure C4. Hysteresis loops for Pr cylinder with the foliation orientated  $0^\circ$  to the applied field. Raw magnetization (top), and mass normalized moment (bottom).

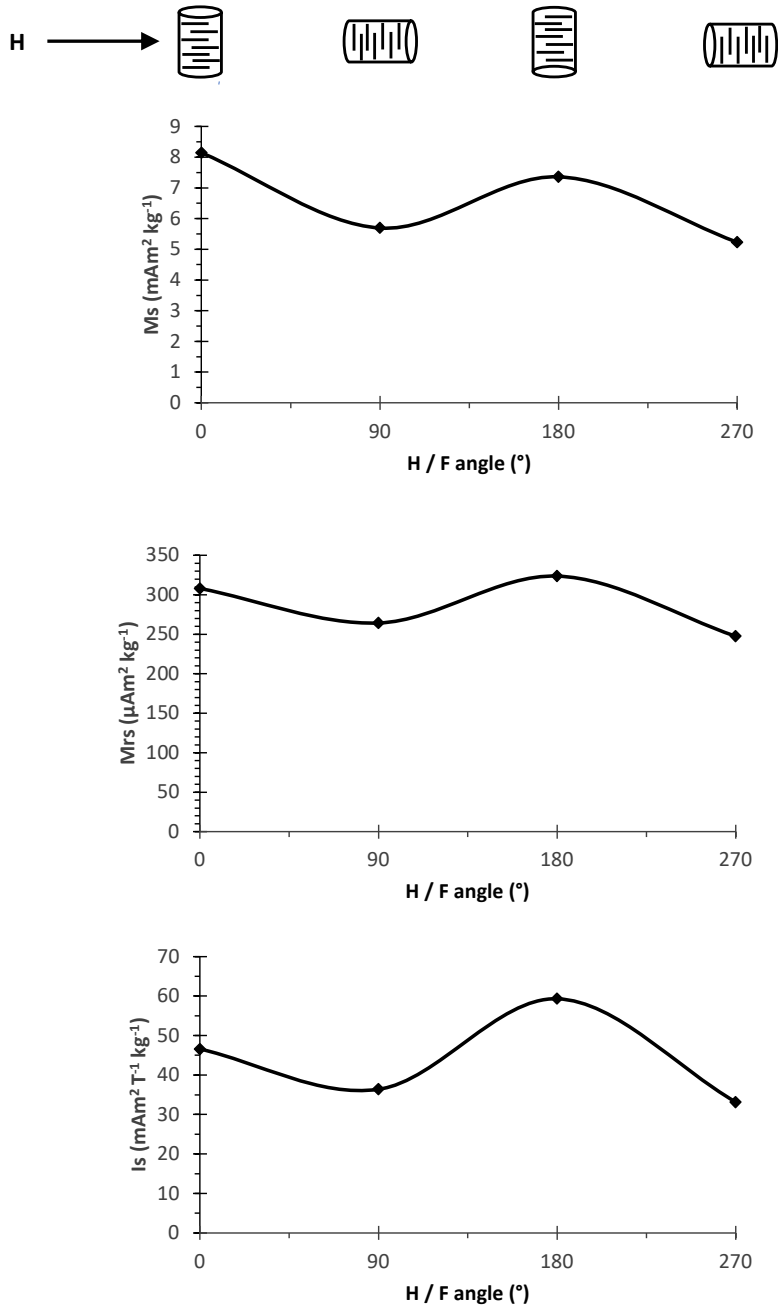


Figure C5. Magnetic concentration parameters for the Pr cylinder with foliation plane positioned at varying angles to the applied field. Magnetic saturation (top), saturation remanence (middle), and initial slope (bottom).

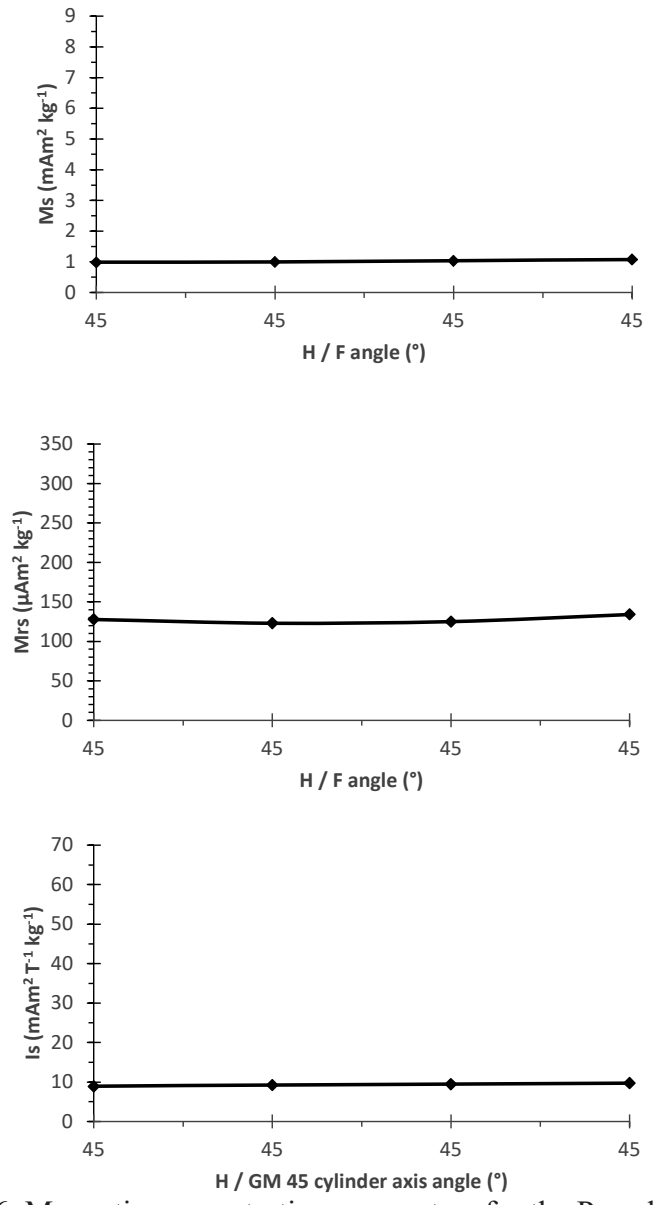


Figure C6. Magnetic concentration parameters for the Pa cylinder with foliation plane positioned at varying angles to the applied field. Magnetic saturation (top), saturation remanence (middle), and initial slope (bottom).

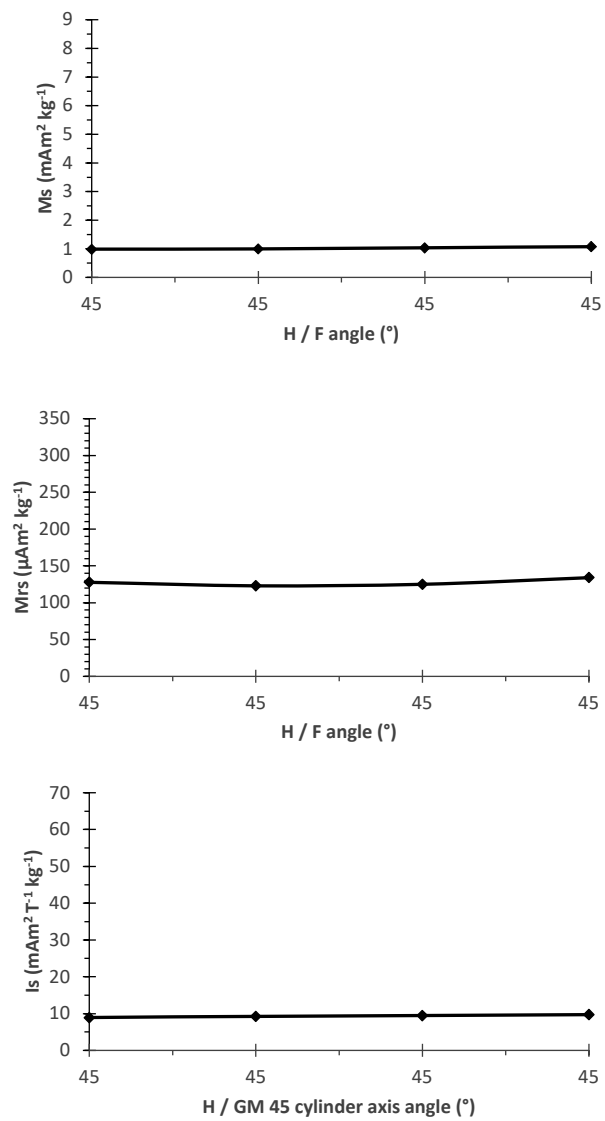


Figure C7. Magnetic concentration parameters for the 45° cylinder with foliation plane positioned at varying angles to the applied field. Magnetic saturation (top), saturation remanence (middle), and initial slope (bottom).

has comparable values of magnetic concentration to the Pa cylinder, but it does not have as much variance with differing orientations (Fig. C7).

### 3.2. Magnetic grain size parameters for Gneiss Minuti cylinders

Since the initial slope of the hysteresis measurement is comparable to susceptibility of magnetization, the parameter of saturation remanence divided by initial slope  $M_{rs}/I_s$  is comparable to the grain size parameter of saturation remanence divided by susceptibility ( $M_{rs}/\chi$ ) (App. CA). The Pr cylinder obtained lower values of  $M_{rs}/I_s$  than the Pa and 45° cylinders, suggesting that it has a coarser magnetic grain size (Fig. C8). The Pr and Pa cylinders demonstrate a variance in the  $M_{rs}/I_s$  parameter in relation to foliation orientation to the applied field, being consistently larger in value for the 90° and 270° orientations (foliation perpendicular to the field). The 45° cylinder does not display a systematic variance. A plot of  $M_{rs}/M_s$  over  $H_{cr}/H_c$  (Day plot, App. CA), further characterizes the difference between the three cylinders, with the Pr cylinder plotting in the multi-domain range and the Pa and 45 cylinder plotting in the pseudo single domain range (fig. C9). A first order reversal curve (FORC) done for the Pr cylinder is in agreement with its position on the day plot, showing a multi-domain pattern (Fig. C10).

### 3.3. Magnetic mineralogy parameters for Gneiss Minuti cylinders

The three cylinders have comparable values of coercivity of remanence ( $H_{cr}$ ), with all being in the range of 20 – 30 mT, suggesting that a low coercivity magnetic mineral phase is present (App. A, fig. C11). The  $H_{cr}$  of the Pr and Pa cylinders vary with the changes in foliation angle to the applied field whereas the 45° cylinder is relatively constant. The Pr and Pa cylinder variance is systematic, with the harder (higher coercivity) orientation being perpendicular to the foliation (90° and 270°) (Fig. C11). The  $H_{cr}$  values for the Pa cylinder in the 45° and 135° positions display intermediate values compared to angles associated with foliation perpendicular or parallel positions. There is also some variation in  $H_{cr}$  values for the Pa cylinder in the 0° position but rolled about its

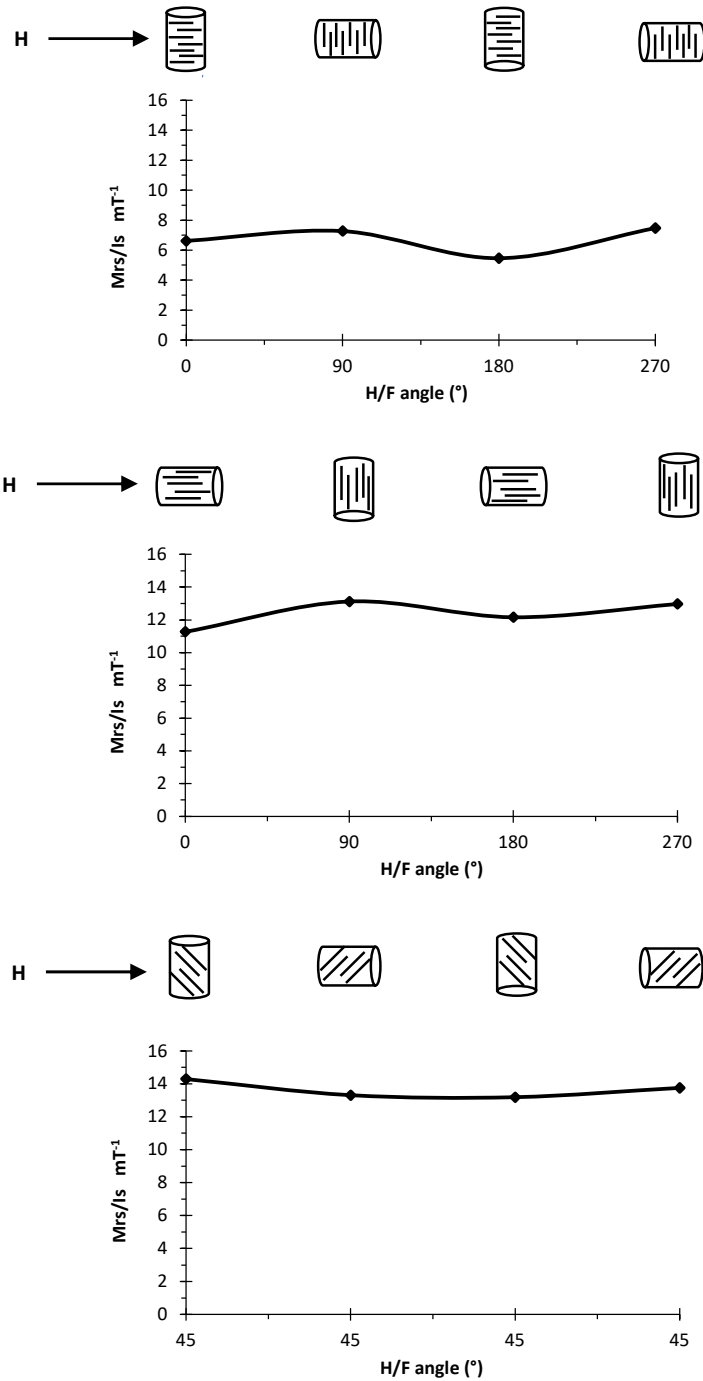


Figure C8. Mrs/Is (saturation remanence over initial slope) Higher values indicate larger grain size. Pr cylinder (top) Pa cylinder (middle), and 45° cylinder (bottom).

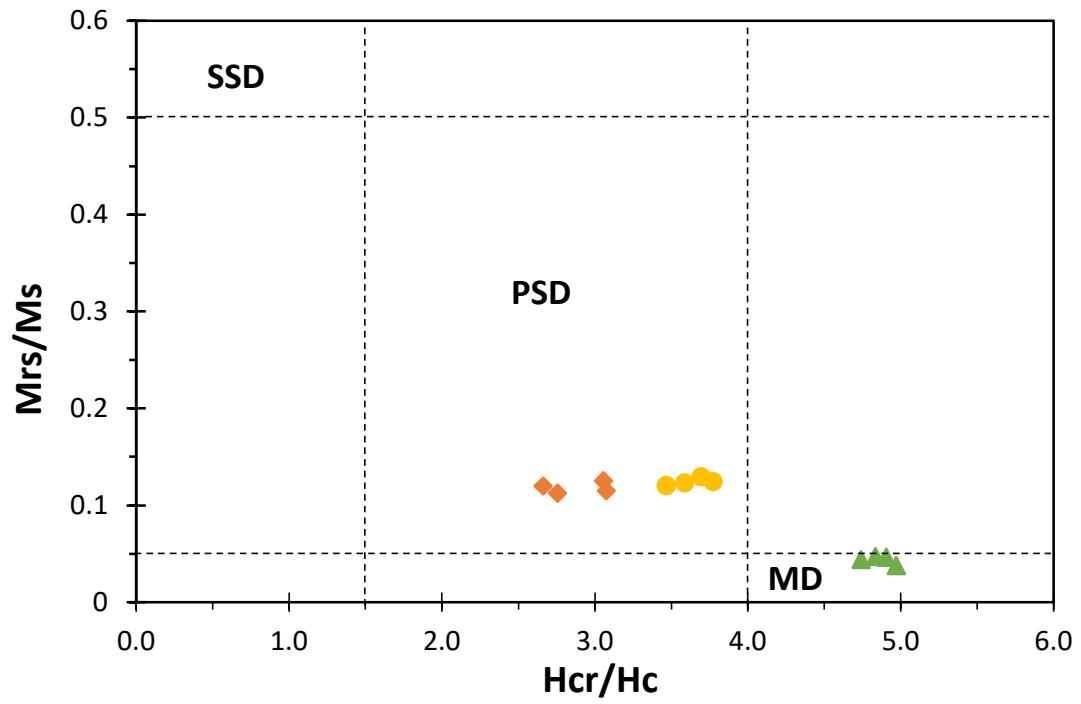


Figure C9. Day plot (grain size parameter) of Pr cylinder (triangles) Pa cylinder (diamonds) and 45° cylinder (circles).

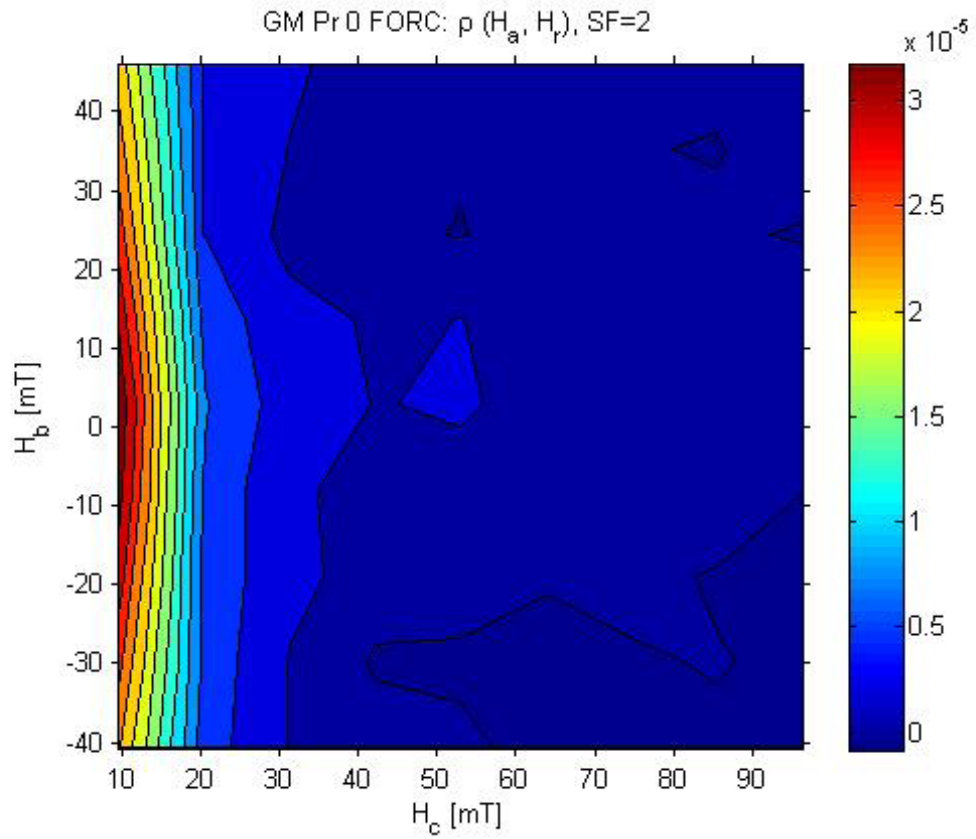


Figure C10. First order reversal curve (FORC) of the Pr cylinder, indicating a multi-domain pattern.

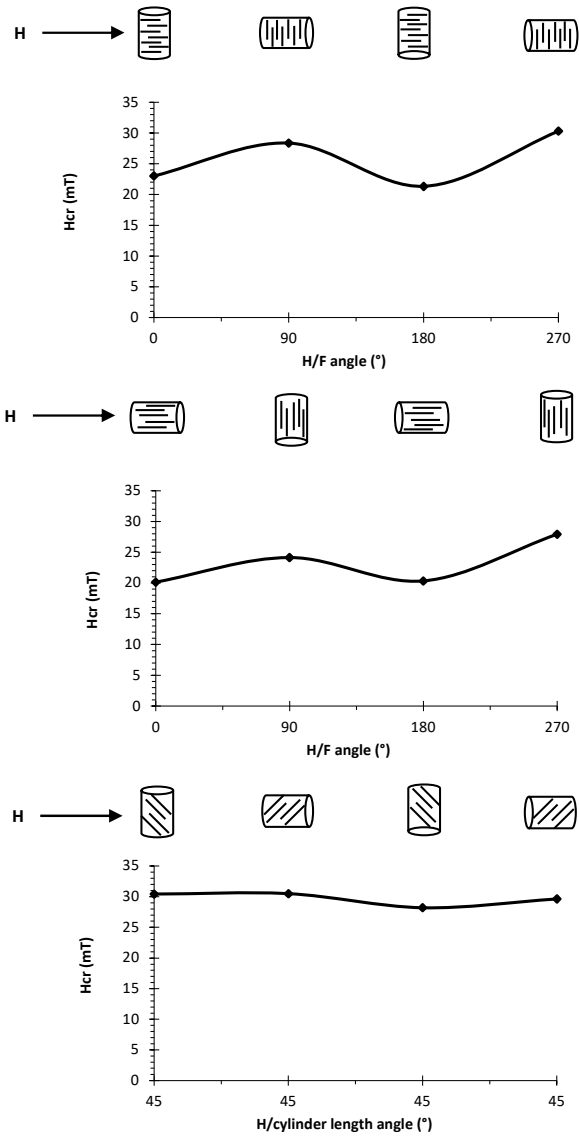


Figure C11. Fig. 11. Hcr for cylinders at varying angles to the foliation. Pr cylinder (top) Pa cylinder (middle) and 45 cylinder (bottom).

axial plane 45° and 90° (Fig. C12). All cylinders in all orientations demonstrate a similar pattern of isothermal remanence magnetization (IRM) acquisition between 70 and 80% of remanence is gained by 100mT, and by 300mT close to 100% saturation remanence is acquired, showing the presence of a low coercivity phase (Fig. C13). For all samples in all orientations, an S-ratio was acquired by dividing the IRM value at 300mT by the IRM value at 500mT. All values range between 0.96 and 1.00. This is indicative of an easily magnetizable phase such as magnetite (App. CA, table C2).  $H_{cr}'/H_{cr}$  values were between 2.1 and 2.8, indicating that there is likely no titanium present (App CA, Table C2).

#### 3.4 Biotite and phlogopite

The hysteresis measurements for the biotite sample indicate that it is paramagnetic, while the phlogopite is diamagnetic (Figs. C14 and C15). Magnetic saturation ( $M_s$ ) and initial slope ( $I_s$ ) remain relatively constant for all orientations of biotite (Figs. C16 and C17). For the 90° rotation of the basal plane, saturation remanence ( $M_{rs}$ ) remains constant while there is an increase in coercivity of remanence ( $H_{cr}$ ), showing that the harder orientation for biotite is perpendicular to its basal plane. For the rotations of the A/B axes, there an increased value for  $M_{rs}$  in the 45° rotated position.

### 4. Discussion

#### 4.1. Magnetic Properties of Gneiss Minuti Cylinders

The magnetic mineralogy parameters indicate that the three gneiss minuti cylinders contain ferrimagnetic minerals. They have low coercivity of remanence values, and the IRM acquisition pattern is consistent with a low coercivity mineral. It is characteristic of ferrimagnetic minerals such as magnetite to obtain 70% or more of their saturation remanence after being subjected to a field of 100mT, and 100% by ~300mT (Evans and Heller, 2003, p. 44). S-ratios for all cylinders indicate ferrimagnetic content, such as magnetite (App. CA, table C2). Furthermore, the low field and high field slope

Table C2. Magnetic mineralogy parameters for Gneiss Minuti cylinders.

Sample	H/F angle (°)	Low field slope $\mu\text{Am}^2 \text{T}^{-1} \text{kg}^{-1}$	High field slope $\mu\text{Am}^2 \text{T}^{-1} \text{kg}^{-1}$	Low - high $\mu\text{Am}^2 \text{T}^{-1} \text{kg}^{-1}$	% ferri	Hcr (mT)	Hcr' (mT)	S-ratio	Hcr'/Hcr
Pr 0	0	1.10	0.81	0.29	26.7	23.03	64.47	0.97	2.80
Pr 90	90	0.97	0.73	0.24	25.0	28.37	70.70	0.96	2.49
Pr 180	180	1.11	0.79	0.32	28.9	21.34	61.63	0.97	2.89
Pr 270	270	0.96	0.73	0.22	23.3	30.32	69.63	0.98	2.30
Pa 90	0	0.77	0.71	0.06	7.4	20.15	55.63	1.00	2.76
Pa 180	90	0.65	0.60	0.05	7.7	24.15	56.27	0.98	2.33
Pa 270	180	0.75	0.70	0.06	7.4	20.33	57.56	0.99	2.83
Pa 0	270	0.70	0.66	0.04	5.9	27.92	63.34	0.98	2.27
45 0	45	0.33	0.30	0.04	10.7	30.43	65.64	1.00	2.16
45 90	45	0.30	0.28	0.02	6.7	30.49	66.50	0.98	2.18
45 180	45	0.33	0.31	0.02	6.0	28.21	65.31	0.99	2.32
45 270	45	0.30	0.28	0.02	6.5	29.63	66.21	0.98	2.23

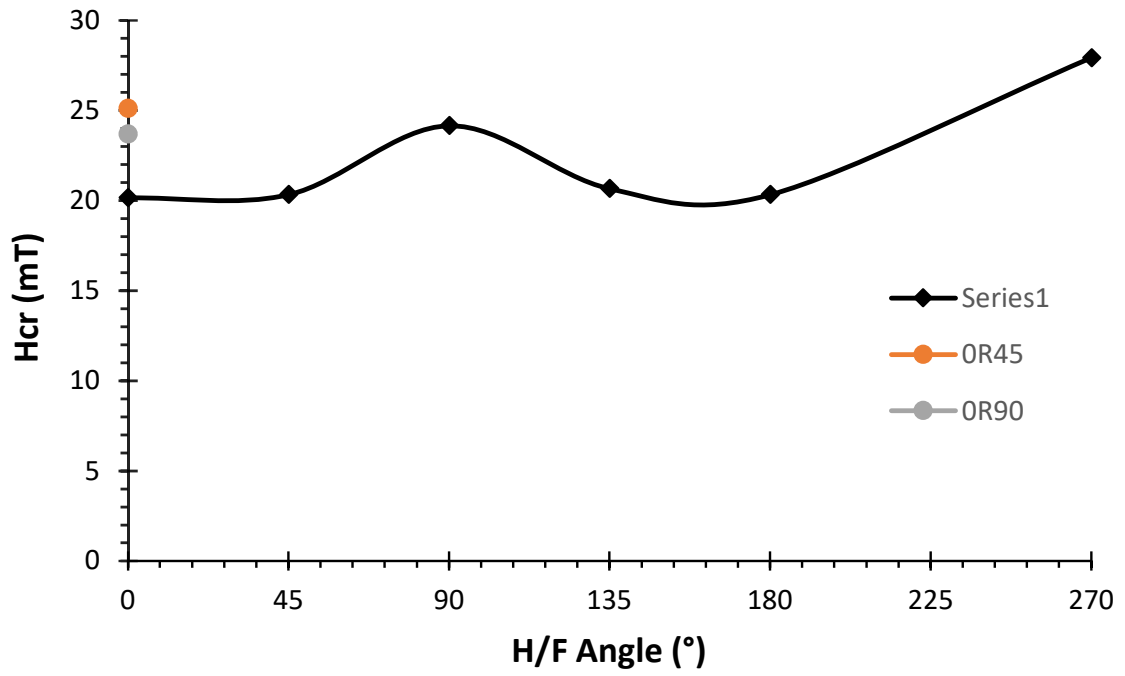


Figure C12. Hcr of Pa cylinder with 45° and 135° angles as well as the two 0° “rolls”.

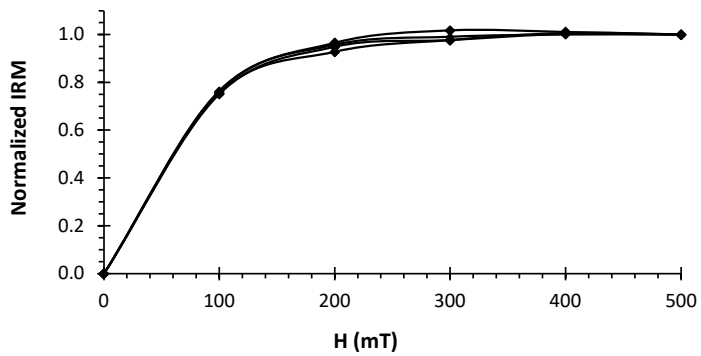
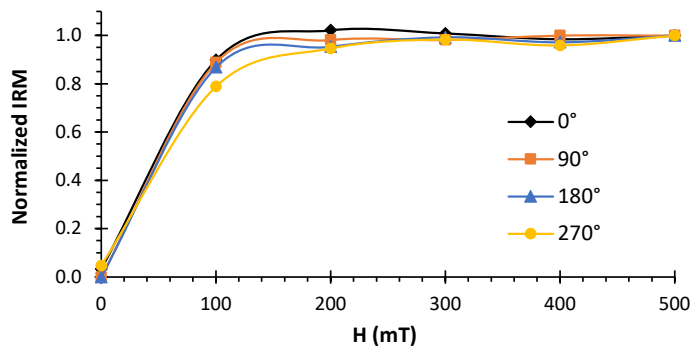
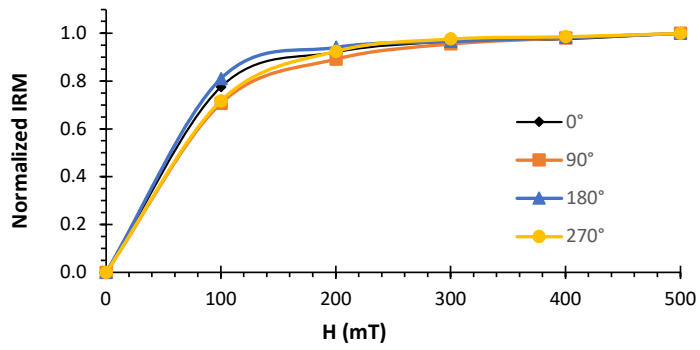


Figure C13. IRM acquisition curves for the three cylinders in all orientations. Pr cylinder (top), Pa cylinder (middle) and 45° cylinder (bottom).

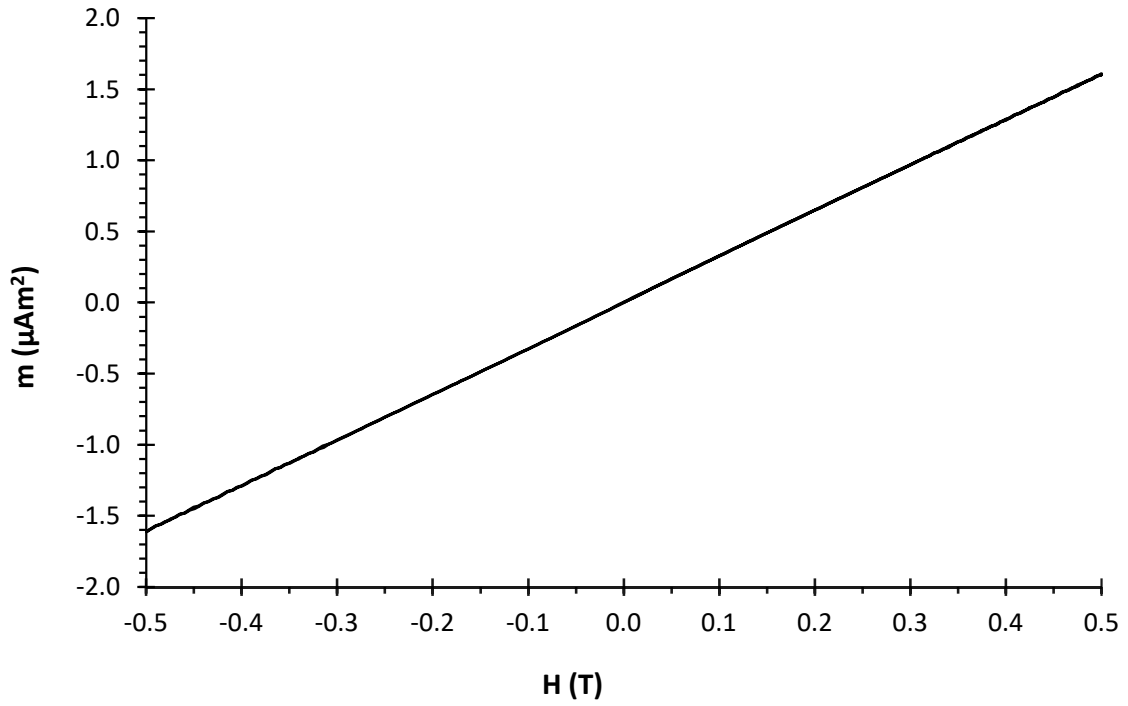


Figure C14. Hysteresis loop for biotite with the basal plane orientated at  $0^\circ$  to the applied field.

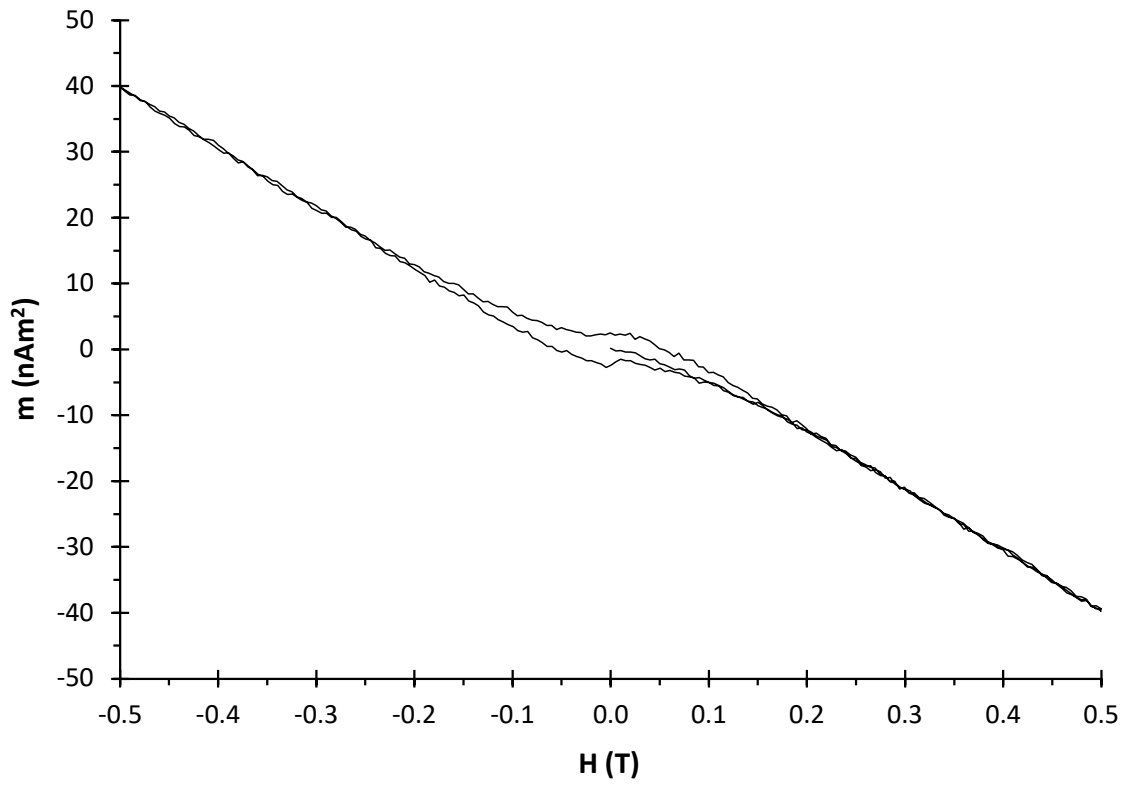


Figure C15. Hysteresis loop of phlogopite with basal plane orientated at  $0^\circ$  to the applied field.

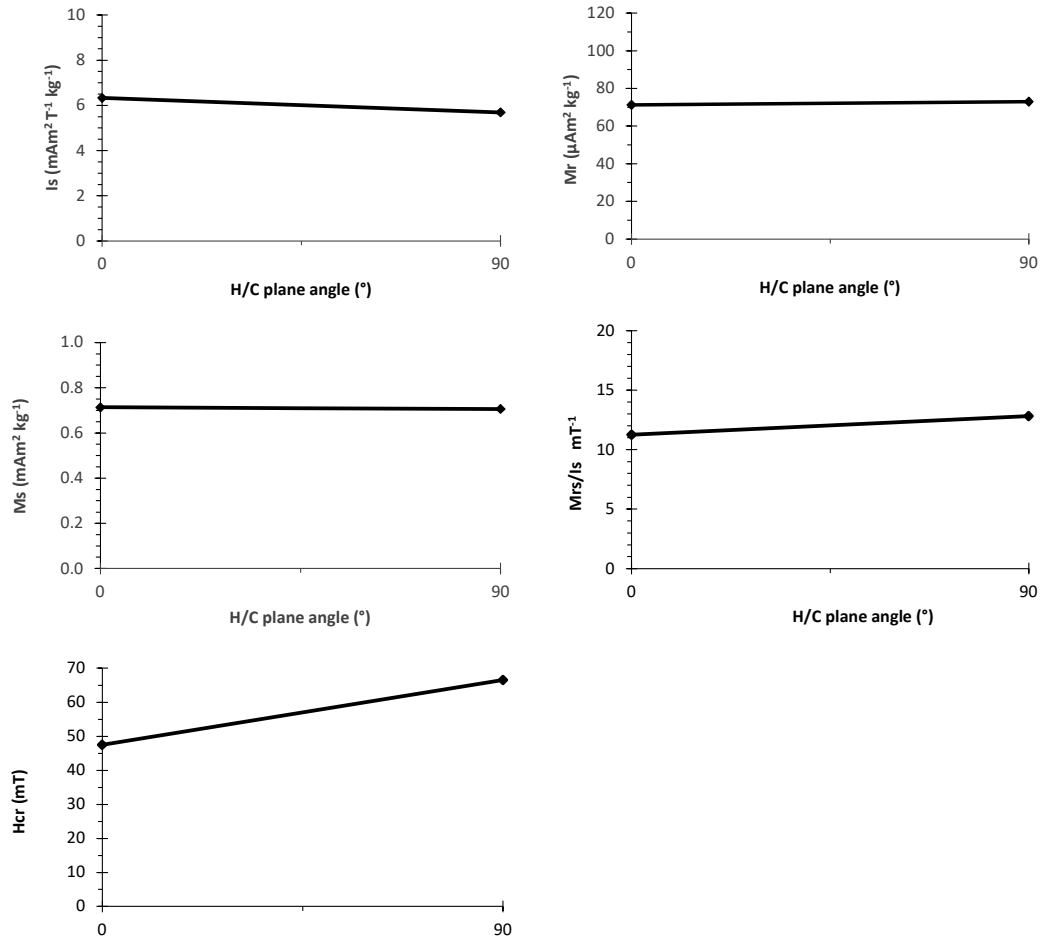


Figure C16. Biotite parameters with the basal plane oriented at 0 and 90° to the applied field.

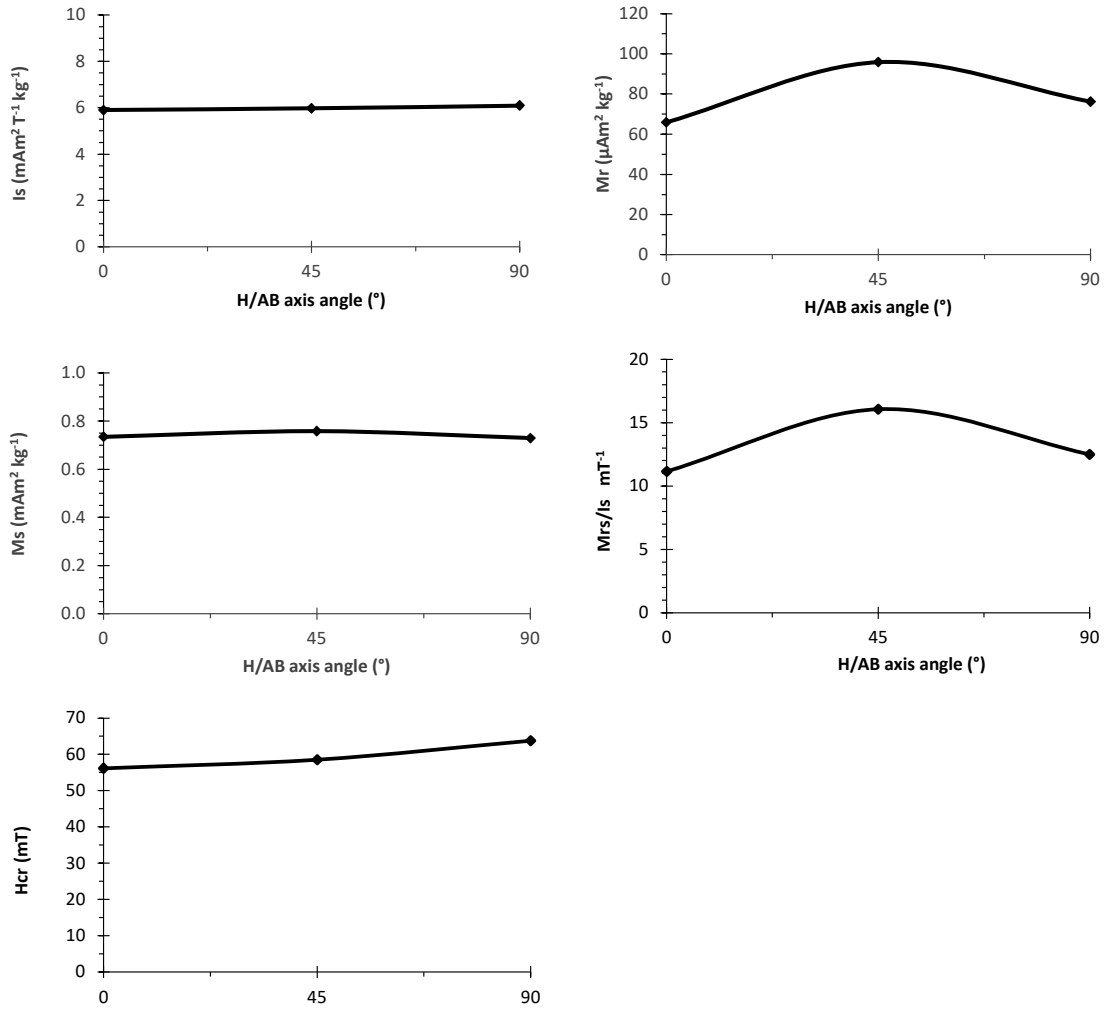


Figure C17. Biotite parameters with the AB axes at various angles to the applied field.

comparisons indicate that there is a ferrimagnetic contribution to the low field slope. Dividing the low field slope by the difference between the low and high field slopes yields a percentage of ferrimagnetic contribution, which varied by orientation but was much greater for the Pr cylinder (~25%) than the Pa and 45° cylinders (~7%) (Table C2). The most likely explanation for ferrimagnetic content is that oxide grains observed in the SEM and petrographic microscope are magnetite.  $H_{cr}'/H_{cr}$  values suggest that there is no Ti content, however this could be further assessed using SEM X-ray analysis (App CA, Table C2).

The magnetic grain size within the cylinder ranges from pseudo single domain to multi domain. Of the three cylinders, the Pr cylinder is interpreted to have the coarsest magnetic grain size, as it displays the lowest values of  $M_{rs}/I_s$  (App. CA, fig. C5). This is consistent with the placement of the Pr cylinder within the multi domain region of the Day plot, while the Pa and 45° cylinders plot in the pseudo single domain region, indicating that they have a finer grain size. Mixtures of superparamagnetic and more stable (pseudo single and single domain) grain sizes may confound the accuracy of the day plot, however the plotting of the Pr cylinder in the multidomain range is also consistent with its first order reversal curve (FORC) diagram, which indicates multidomain behavior (fig. 10).

The Pr cylinder displays the highest magnetic concentration, which may be partially explained by the grain size parameters obtained for this cylinder. Optical and SEM images of the gneiss minuti indicate that there are less than 1% oxides evenly dispersed throughout the layer, with most grains between 10 and 60 $\mu$ m in diameter (fig. C2). The larger grains would likely fall into the realm of multi – domain grain size; magnetic grains can depart from pseudo single domain characteristics even after around 1 $\mu$ m (Evans and Heller, 2003, p. 17). Given the dimensions of the cylinders (1.5mm diameter, ~3mm length), relatively significant variations of oxide content within a given cylinder

can be expected. The concentration variations between the three cylinders is attributed to the intersection of varying quantities and sizes of oxide grains.

While the biotite does display some variation in magnetic properties with orientation to the field, it has no remanence, making it paramagnetic (figs. 14, 16 and 17). Biotite may act like a remanence bearing mineral when there are inclusions of magnetite in the biotite (Dunlop and Ozdemir, 1997, p. 80-81). However, this does not appear to be the case for the measured biotite samples. Barring the possibility of magnetite inclusions within the Gneiss Minuti biotite, it is likely that biotite orientation has no effect on the magnetic characteristics of the Gneiss Minuti.

#### 4.2 Magnetic Anisotropy

Both the Pr and the Pa cylinder are higher in all concentration parameters and lower in coercivity of remanence when the foliation is orientated at  $0^\circ$  and  $180^\circ$  to the field, indicating that that the easiest magnetization direction is parallel with the foliation. The anisotropy of the concentration parameters of the Pa cylinder is less pronounced than the Pr cylinder, which is attributed to the Pa cylinder being significantly lower in concentration of ferrimagnetic content. However, the anisotropy of coercivity remanence of the Pa cylinder is nearly as pronounced as that of the Pr cylinder (fig C8). This can be expected since  $H_{cr}$  values are not dependent on concentration. Since the  $45^\circ$  cylinder was measured with the foliation at  $45^\circ$  to the field in all orientations, it does not display any variation in  $H_{cr}$  values with the different orientations.

Elongate grains are most easily magnetized along their long axis. Biotite grains are elongate parallel to the foliation of the gneiss minuti while quartz, plagioclase grains are relatively equant. However, the thin section and SEM images of the Gneiss Minuti layer used in this study show that many of the oxide grains are elongate in the direction of the foliation (Fig C2). The shape of these grains is a possible explanation for the observed magnetic anisotropy. Mamtani et al. (2011) examined the magnetic anisotropy of a

deformed granite by performing anisotropy of anhysteretic remanence magnetization (AARM) on cylinders. The granite did not have a visible foliation, but they were able to identify a magnetic foliation plane defined by an orientation of higher ARM values, and an orientation with lower ARM values perpendicular to it. The magnetic anisotropy was attributed to a shape preferred orientation (SPO) of magnetite grains. Electron backscatter diffraction (EBSD) analysis revealed that the grains had not been subjected to crystal plastic deformation, but rather had been rigidly rotated into an alignment of their long axes. By comparing differences of AARM from varying locations, Mamtani et al. (2011) were able to identify a regional strain gradient. The gneiss used in this study is much more highly strained than the granite studied by Mamtani et al. (2011), so they may not be directly comparable. Quantification of the shape orientation of oxide grains in the Gneiss Minuti would help to better understand how this attribute affects the magnetic characteristics.

Another possible explanation of the anisotropy is a lattice preferred orientation of magnetite grains in relation to the foliation. There is a lattice preferred orientation of quartz grain in the Gneiss Minuti as a result of ductile deformation (Handy, 1986), and it may be possible that oxide grains have been subjected to ductile deformation as well. Magnetic anisotropy as a result of lattice preferred orientation can be observed in the case of hematite crystals subject to deformation. Deformation can cause them to be orientated with the C axes perpendicular to foliation, which would lead to increased susceptibility parallel to foliation (Dunlap and Ozdemir, 1997, p. 485-486). A lattice preferred orientation of magnetite would likely lead to magnetic anisotropy, however the determination of a lattice preferred orientation of the oxide grains in the Gneiss Minuti is beyond the extent of this study.

## 5. Conclusions

Based on the information gained from this study and its comparison with previous studies, the following conclusions are made.

1. The Gneiss Minuti contains a ferrimagnetic mineral, which is likely titanium free magnetite.

2. There is a significant variation in magnetic concentration between the three cylinders, with the Pr cylinder having more magnetite than the Pa and 45° cylinders. This variation in magnetite can be attributed to varying grain size and quantities of oxide grains within each cylinder as a result of core placement.

3. The magnetic properties of the Gneiss Minuti display systematic variation when compared to the foliation plane, showing higher remanence and lower coercivity parallel to foliation. There seems to be a distinct magnetic anisotropy as a result of metamorphic texture, with the easy orientation parallel with the foliation.

4. The anisotropy is likely the result of a shape preferred orientation of oxide grains, which are slightly oblong, with the long axes parallel to foliation. It is also possible that ductile deformation of oxide grains resulting in a lattice preferred orientation contributes to the observed anisotropy.

#### 6. Further Study

Several directions of further research should be conducted to better understand the magnetic anisotropy of the Gneiss Minuti. It would be helpful to conduct the same experiments but on a larger number of samples. Both the Pa cylinder and 45° cylinder were very low in magnetic concentration to the Pr cylinder, which is attributed to the dispersed nature of the oxide grain within the Gneiss Minuti. A larger number of samples in all orientations would help to make a more representative analysis of the material and would be likely to further support the observations of magnetic anisotropy.

Elemental analysis via scanning electron microscope (SEM) or phase analysis via X-ray diffraction (XRD) could also be conducted to further delineate the presence

magnetite and other remanence bearing iron oxides, as well as to assess titanium content. Electron backscatter diffraction (EBSD) could be conducted to identify the mechanism and extent of deformation of magnetite grains, as well as a lattice preferred orientation which could contribute to the observed magnetic anisotropy. It would also be useful to further characterize the shape of the oxide grains within the Gneiss Minuti to better understand the extent of their shape preferred orientation.

#### Acknowledgments

The author would like to thank Dr. John Peck for clear minded guidance on research strategies. The author would also like to thank Dr. Caleb Holyoke for providing the Gneiss Minuti samples, John Fox for providing the biotite and phlogopite samples, and Tom Quick for assistance with the use of the AGM apparatus.

## References

- Dunlop, D. J., & Özdemir, O. (1997). *Rock magnetism: Fundamentals and frontiers*. Cambridge: Cambridge University Press.
- Evans, M. E., & Heller, F. (2003). *Environmental magnetism: Principles and applications of enviromagnetics*. Amsterdam: Academic Press.
- Gottschalk, R. R., A. K. Kronenberg, J. E. Russell, and J. Handin (1990), Mechanical Anisotropy of Gneiss - Failure Criterion and Textural Sources of Directional Behavior, *J Geophys Res-Solid*, 95(B13), 21613-21634, doi:DOI 10.1029/JB095iB13p21613.
- Handy, M.R., 1986. The structure and rheological evolution of the Pogallo Fault Zone, a deep crustal dislocation in the Southern Alps of Northwestern Italy. Ph.D. Thesis, Univ. of Basel, 327 pp.
- Mamtani M.A., S. Piazzolo, R.O. Greiling, A. Kontny, and F. Hrouda (2011), Process of magnetite fabric development during granite deformation, *Earth Planet. Sci. Lett.* 308, 77-89, doi.org/10.1016/j.epsl.2011.05.033.
- Zurbriggen, R., B. S. Kamber, M. R. Handy, and T. F. Nagler (1998), Dating synmagmatic folds: a case study of Schlingen structures in the Strona-Ceneri Zone (Southern Alps, northern Italy), *J Metamorph Geol*, 16(3), 403-414, doi:DOI 10.1111/j.1525-1314.1998.00145.x.

Appendix C.A. Magnetic parameters and their interpretation.  
Magnetic concentraion parameters

Parameter	Interpretation	Limits
Sucseptibility (X)	A larger value signifies more ferrimagnetic content	Measured in a field so there is a contribution from diamagnetic and paramagnetic  Mass susceptibility considers changes in density, volume susceptibility does not  Grain size can have an affect on susceptibility
Anhyseretic remanent magnetization (ARM)	The higher the value the more ferrimagnetic material	Biased to SSD and PSD particles because of the easy movement of domain walls in MD particles  Afected by mineralogy; ferrimagnetic minerals have greater effect
Saturation isothermal remanent magnetization (SIRM)	The higher the value the more ferrimagnetic material	Biased to SSD and PSD particles because of the easy movement of domain walls in MD particles  Afected by mineralogy; ferrimagnetic minerals have greater effect
Magnetic saturation ( $M_s$ )	The higher the value the more ferrimagnetic material	Independent of grain size  Afected by mineralogy; ferrimagnetic minerals have greater effect

Appendix C.A. (Continued)  
Magnetic grain size parameters

Parameter	Interpretation	Caution
Frequency dependence of susceptibility ( $\chi_{fd}$ )	A value greater than 2% indicates SPM grains	The low frequency value ( $\chi_{lf}$ ) needs to be in the high teens (>15), or the measurement will be affected by random noise
Hysteresis loop shape	A wider loop indicates finer grain size	Can be affected by mineralogy or grain size mixtures  SPM grains have no loop
Day Plot ( $M_{rs}/M_s$ vs. $H_{cr}/H_c$ )	SSD particles are graphed at high $M_{rs}/M_s$ values and low $H_{cr}/H_c$ values. MD particles are graphed at high $H_{cr}/H_c$ values and low $M_{rs}/M_s$ values	Functions best when material tested is known to be dominantly magnetite. Variations in mineralogy will affect the plot due to the different magnetic properties of magnetite and hematite
FORC diagram	Various shapes of the diagram correspond to different particle sizes. SD particles result in . horizontally elongate contours, MD particles have verticle contours.	
Alternating field demagnetization	SSD grains are more resistant to demagnetization than MD grains	A mixture of SPM and SSD grains can give a low ratio similar to MD grains
SIRM/ $\chi$	Larger ratio signifies more fine grained particles	A mixture of SPM and SSD grains can give a low ratio similar to MD grains
$\chi_{arm}/\chi$	Larger ratio signifies more fine grained particles	A mixture of SPM and SSD grains can give a low ratio similar to MD grains
$\chi_{arm}/SIRM$	Larger ratio signifies more fine grained particles	A mixture of SPM and SSD grains can give a low ratio similar to MD grains

Appendix C.A. (Continued)  
Magnetic mineralogy parameters

Parameter	Interpretation	Caution
Hysteresis loop shape	A tall narrow loop signifies magnetite because it has high $M_s$ and low $H_c$ . A short wide loop signifies hematite because it has low $M_s$ and high $H_c$	Grain size will affect the shape of the loop
$H_{cr}$	Hematite has a much greater coercivity of remanence than magnetite	Grain size will have an affect on this; SSD grains have more coercivity
Isothermal remanent magnetization (IRM) acquisition	Magnetite reaches $M_{rs}$ at $\approx 300$ mT. Hematite reaches $M_{rs}$ at $\approx 2500$ mT. Goethite reaches $M_{rs}$ at $\approx 7000$ mT	
$H_{cr}'/H_{cr}$	1.6 $\pm$ .2 signifies magnetite 1.2 $\pm$ .2 signifies titanomagnetite 1 signifies hematite	Coercivity is affected by grain size mineralogic and grain size mixtures can confound data
S ratio	The proportion of IRM at 300 mT to the SIRM will signify the proportion of magnetite to hematite. 1 = all magnetite, 0.9 $\approx$ 50 % hematite, 0.5 $\approx$ mostly hematite	
HIRM	Signifies amount of hematite/goethite (non ferrimagnetic magnetic minerals)	HIRM value can easily be swamped by magnetite
Sulfide biplot	Distinguishes between magnetite and sulfides based on where they plot	Mixtures can confound the data
Stability vs. squareness plot	Distinguishes between high and low coercivity minerals as well as grain size	